



1 Aerosols-precipitation elevation dependence over the Central
2 Himalayas using cloud-resolving WRF-Chem numerical
3 modeling

4

5 Pramod Adhikari^{1,2} John F. Mejia^{1,2}

6

7 ¹ *Division of Atmospheric Sciences, Desert Research Institute, Reno, Nevada, USA*

8 ² *Atmospheric Sciences Graduate Program, University of Nevada, Reno, Nevada, USA*

9

10 Correspondence to: John F. Mejia (john.mejia@dri.edu) and Pramod Adhikari (adhik.pramod@nevada.unr.edu)

11



12 **Abstract**

13 Atmospheric aerosols can modulate the orographic precipitation impacting the evolution of clouds through radiation
14 and microphysical pathways. This study implements the cloud-resolving Weather Research and Forecasting model
15 coupled with chemistry (WRF-Chem) to study the response of the Central Himalayan elevation-dependent
16 precipitation to the atmospheric aerosols. The first monsoonal month of 2013 is simulated to assess the effect of
17 aerosols through radiation and cloud interactions. The results show that the response of diurnal variation and
18 precipitation intensities (light, moderate, and heavy) to aerosol radiation and cloud interaction depended on the
19 different elevational ranges of the Central Himalayan region. Below 2000 m ASL, the total effect of aerosols
20 resulted in suppressed mean light precipitation by 19% while enhancing the moderate and heavy precipitation by 3%
21 and 12%, respectively. In contrast, above 2000 m ASL, a significant reduction of all three categories of precipitation
22 intensity occurred with the 11% reduction in mean precipitation. These contrasting altitudinal precipitation
23 responses to the increased anthropogenic aerosols can significantly impact the hydroclimate of the Central
24 Himalayas, increasing the risk for extreme events and influencing the regional supply of water resources.

25



26 1. Introduction

27 The south Asian summer monsoon system, one of the major monsoonal systems on Earth, is located in the
28 region with the persistent occurrence of substantial loadings of atmospheric aerosols (Li et al., 2016). The densely
29 populated and rapidly growing urban centers of the Indo-Gangetic Plain (IGP), located over northern India at the
30 foothills of the Himalayas, experience frequent events of severe air pollution with significant contribution from local
31 anthropogenic activities and remotely transported mineral dust aerosols (Dey and Di Girolamo, 2011; Kumar et al.,
32 2018; Sijikumar et al., 2016). Atmospheric aerosols, from both natural and anthropogenic sources, can impact the
33 weather and climate on a local to global scale through interactions with radiation and cloud, as well as through
34 albedo and hydrologic pathways due to deposition over the snow (e.g., Sarangi et al., 2019; Wu et al., 2018;
35 Andreae and Rosenfeld, 2008; Haywood and Boucher, 2000; Mahowald et al., 2011; Ramanathan and Carmichael,
36 2008). However, due to inhomogeneous distribution and complex radiation and cloud interaction, aerosol also
37 contributes to the larger uncertainties in assessing the Earth's changing climate (IPCC, 2013).

38 The Aerosol-Radiation Interaction (ARI) comprises the direct radiative effects, which include the scattering
39 and absorption of solar radiation depending on the optical properties, and the semi-direct effect (IPCC, 2013). The
40 semi-direct effect refers to the heating of the cloud due to the absorbing aerosols, which reduces the relative
41 humidity and increases the cloud burn-off process resulting in lower planetary albedo (Hansen et al., 1997; Huang et
42 al., 2006a; Ackerman et al., 2000). The ARI can alter the surface energy budget, atmospheric thermodynamic
43 structure, convective stability, and tropical-meridional circulation, in turn modulating the frequency and intensity of
44 the monsoonal rainfall (e.g., Li et al., 2016; Ramanathan et al., 2005; Lau et al., 2006). At a daily timescale, due to
45 the direct radiative effect increases the low-level stability over the polluted urban plains resulting in enhanced
46 moisture transport towards the downwind mountains and abnormally increasing precipitation (Choudhury et al.,
47 2020; Fan et al., 2015).

48 IPCC (2013) refers to the Aerosol-Cloud Interaction (ACI) to the modification of cloud microphysical
49 properties or cloud evolution through the ability of aerosol to act as cloud condensation nuclei (CCN) or Ice-
50 Nucleating particles (INPs). Polluted clouds or clouds with a higher concentration of CCN increase the number of
51 smaller cloud droplets for a constant liquid water path and enhances the reflection, also known as the first indirect
52 effect (Twomey, 1977). Smaller cloud droplets result in increased cloud lifetime and height and suppress the drizzle
53 precipitation, also known as the second indirect or cloud lifetime effect (Pincus and Baker, 1994; Albrecht, 1989;
54 Rosenfeld, 1999). The continuing and intensified updrafts with the release of latent heat of condensation and
55 freezing and additional thermal buoyancy invigorate the convection strength and cloud development (Rosenfeld et
56 al., 2008; Andreae et al., 2004; Koren et al., 2005). Additionally, Fan et al. (2017) proposed that the increase in
57 latent heat release with CCN concentration strengthens the moisture transport to the windward slope and can
58 invigorate the mixed phase orographic clouds resulting in higher precipitation over the Sierra Nevada, California.

59 The locally emitted and transported anthropogenic aerosols can impact the precipitation, vertical
60 temperature distribution, and regional hydroclimate of the Himalayan and the adjacent region. The deep convective
61 activity and southwesterly monsoonal flow incorporate the remote dust and anthropogenic aerosols from the IGP



62 and transports them to the southern slopes of the Himalayas and even to the Tibetan Plateau (Kang et al., 2019; Ji et
63 al., 2015; Vernier et al., 2011). Adhikari and Mejia (2021) indicated that the heavier aerosol loadings contribute to
64 the increased freezing isotherm over the Central Himalayas during the monsoonal season. The increasing trend of
65 the freezing level height (FLH) has been reported around the globe (e.g., Wang et al., 2014; Bradley et al., 2009;
66 Zhang and Guo, 2011; Prein and Heymsfield, 2020; Lynn et al., 2020), and can impact the snowline altitude (Wang
67 et al., 2014; Prein and Heymsfield, 2020). The amplified warming of the mountainous terrain or the elevation-
68 dependent warming around the globe can also be associated with the change in snow cover and albedo, radiative and
69 surface fluxes, changes in water vapor and latent heat release, deposition of aerosols on snowpack, and aerosol
70 concentrations (Pepin et al., 2015; Rangwala et al., 2010). Depending on the location and topographical altitude,
71 different factors can dominate elevation-dependent warming; e.g., the radiative impact of concentrated aerosol
72 loading can play a significant role in modulating the temperature over the slopes of the Himalayas and mid-latitude
73 Asia (Pepin et al., 2015; Rangwala and Miller, 2012; Palazzi et al., 2017).

74 The atmospheric heating due to the accumulated remote dust and carbonaceous aerosols from IGP leads to
75 the northward shift of deep convection and heavier monsoonal rainfall over the foothills of the Himalayas during the
76 early monsoon period (Lau et al., 2006, 2017). Furthermore, the variability in the orographic precipitation has also
77 been linked to the atmospheric aerosols around the globe (Napoli et al., 2019; Wu et al., 2018; Choudhury et al.,
78 2020; Adhikari and Mejia, 2021, 2022). Cho et al. (2016) suggested that anthropogenic climate forcing modifies the
79 circulation structure, triggers the intense rainfall over northern south Asia, and increases the risk of flood severity.
80 Furthermore, long term observational studies by Choudhury et al. (2020) and Adhikari and Mejia (2021) showed
81 that the aerosol invigorated cloud development and enhanced the precipitation over the southern slopes of the central
82 Himalayas. The localized extreme weather events over the complex mountainous terrain pose a higher hazard due to
83 flash floods and landslides.

84 The increased aerosols over the slopes of the Himalayas impacts the microphysical properties of the clouds and
85 can modulate the precipitation pattern over the different elevational band of the Himalayas (Palazzi et al., 2013;
86 Dimri et al., 2022). The climatology of the temperature and precipitation trends and elevational dependence over the
87 Tibetan Plateau (TP) and the Himalayas was recently studied using the climate models (e.g., Palazzi et al., 2017;
88 Ghimire et al., 2018; Dimri et al., 2022), but without including the effect of aerosols. To the best of our knowledge,
89 a study examining the elevation dependence of aerosol-cloud interaction and precipitation response to aerosols over
90 the Central Himalayan region is lacking. A better understanding of aerosol-cloud interaction on elevation-dependent
91 precipitation and temperature of this mountainous region is crucial to assess the hydrologic and climate risks for
92 millions of people residing on the adjacent lowlands. This study seeks to examine whether there is an asymmetrical
93 aerosol-cloud response in the orographic forcing process over the southern slopes of the Himalayas and further
94 estimate and evaluate the role of increased anthropogenic aerosols in modulating the surface temperature
95 distribution along the elevational band. To achieve this goal, we implement the Weather Research and Forecasting
96 (WRF) model coupled with chemistry (WRF-Chem) configured at a cloud-resolving scale, where the organization of
97 the convection is explicitly resolved, for the first monsoonal month of 2013 after the onset of the monsoon in Nepal.
98 To understand the processes involved in the aerosol-cloud interaction and precipitation-elevation dependence, WRF-



99 Chem simulation realizations were performed to isolate the contribution of the ACI and ARI. In section 2, we
100 describe the details of the model used. In section 3, we present and discuss the model evaluation and simulation
101 results. The conclusion of this study is summarized in section 4.

102 **2. Methodology**

103 **2.1 Model description**

104 In this study, we implement the Weather Research and Forecasting (WRF) model coupled with Chemistry
105 (WRF-Chem) version 4.1.5 for numerical simulations (Grell et al., 2005). WRF-Chem is an advanced online
106 coupled regional model which can simulate the emission, transport, and transformation of trace gases and aerosols
107 with atmospheric feedback processes from radiation and meteorology (Chapman et al., 2009; Fast et al., 2006).
108 WRF-Chem consists of several chemistry components, e.g., emission inventories, aerosol-chemistry mechanism,
109 aqueous and gas phase mechanism, dry and wet deposition, and photolysis, and has been widely used to study
110 aerosol-cloud-radiation-climate interaction around the globe (e.g., Wu et al., 2018; Fan et al., 2015; Sarangi et al.,
111 2015; Archer-Nicholls et al., 2016; Liu et al., 2020).

112 The Carbon Bond Mechanism (CBM-Z; Zaveri and Peters 1999), a gas-phase chemistry mechanism coupled
113 with the MOSAIC (Model for Simulating Aerosol Interactions and Chemistry; Zaveri et al. 2008) aerosol module,
114 was utilized. The CBM-Z includes 67 chemical species and 164 reactions and treats the organic compound in a
115 lumped structure approach depending on their internal bond types (Gery et al., 1989; Zaveri et al., 2008). MOSAIC
116 aerosol module simulates all the major aerosol species (including sulfate, nitrate, ammonium, primary organic mass,
117 black carbon, and liquid water) that are deemed to be significant at urban, regional, and global scales (Zaveri et al.,
118 2008). Of note is that the MOSAIC version implemented in this study does not treat the secondary organic aerosols,
119 which are expected to modulate the physical and chemical properties of atmospheric aerosols (Kaul et al., 2011;
120 Hallquist et al., 2009) and can add up the uncertainties in the result. The aerosol size distribution within the
121 MOSAIC aerosol module is represented by a 4 or 8 sectional bin approach. To reduce the computational burden, the
122 aerosol size distribution in the MOSAIC was represented using 4-bins, ranging between 39 nm to 10 μm based on
123 dry particle diameters. The four bin approach reasonably produces similar results in comparison to the eight sized
124 bins approach (Eidhammer et al., 2014; Zhao et al., 2013). All particles within a bin are considered to be internally
125 mixed, which have similar chemical composition, while particles from different sized bins are mixed externally
126 (Zaveri et al., 2008).

127 Composite aerosol optical properties, such as the extinction and scattering coefficient, single scattering albedo,
128 and asymmetry factor, are estimated as a function of the size and chemical composition of aerosols using the volume
129 averaging method with Mie theory (Fast et al., 2006; Chapman et al., 2009). The total integrated aerosol optical
130 properties across all sized bins are then used in the radiation transfer scheme to compute the net radiative effect of
131 aerosols (Chapman et al., 2009; Iacono et al., 2008). The primary aspect of aerosols in impacting cloud evolution
132 and microphysics are the concentration and composition, size distribution, and hygroscopic nature of aerosols
133 (Khain et al., 2016). In a convective cloud, the effect of aerosols on the microphysics is mainly determined by the



134 number of aerosols activated as CCN, which impacts the size and cloud droplet number concentration (Chapman et
135 al., 2009). Aerosols are activated as CCN when the maximum environmental supersaturation is greater than the
136 critical supersaturation of an aerosol, which is a function of aerosol size and composition. The maximum
137 supersaturation of rising air parcels within each size bin is computed as a function of vertical velocity and
138 composition of internally mixed aerosols (Abdul-Razzak and Ghan, 2002). The interstitial aerosols with higher
139 critical supersaturation than maximum ambient supersaturation are not activated as CCN (Chapman et al., 2009).
140 Also, the WRF-Chem can resuspend cloud-borne aerosols to an interstitial state when the cloud particles evaporate
141 within a grid cell (Chapman et al., 2009). The main advantage of using cloud-resolving scales in this aerosol-cloud
142 interacting study is that the activation of aerosols is explicitly resolved by the double-moment microphysics scheme
143 (Archer-Nicholls et al., 2016; Chapman et al., 2009; Yang et al., 2011).

144 This study uses the anthropogenic emission inventories from the Emission Database for Global
145 Atmospheric Research-Hemispheric Transport of Air Pollutants (EDGAR-HTAP) and EDGARv4.3.2 (Janssens-
146 Maenhout et al., 2015). EDGAR-HTAP is a global monthly emission inventory for the year 2010 at a spatial
147 resolution of $0.1^\circ \times 0.1^\circ$. EDGAR-HTAP emission inventory includes the black carbon, organic matter, particulate
148 matter, ammonia, sulfates, oxides of nitrogen, and carbon monoxide, from the major anthropogenic sources from
149 power generation, industry, residential, agriculture, ground and aviation transport, and shipping. The non-methane
150 volatile organic compounds in this study are provided from EDGARv4.3.2. This study utilizes the biogenic
151 emissions from the Model of Emissions of Gases and Aerosols from Nature (MEGAN), which quantifies the net
152 emissions from the terrestrial biosphere at a horizontal resolution of one square km (Guenther et al., 2006, 2012).
153 Fire INventory from NCAR version 1.5 (FINNv1.5), which provides the global estimates of open episodic fires from
154 different sources in a 1 km spatial and daily temporal resolution (Wiedinmyer et al., 2011), is used as biomass
155 burning emissions. Though fire events are less relevant during the monsoon season (2002-2013) in our area of
156 interest (Matin et al., 2017), we used biomass burning information to include all the primary sources of aerosols.

157 The Community Atmosphere Model with Chemistry (CAM-Chem), with $0.9^\circ \times 1.25^\circ$ spatial resolution
158 with 56 vertical levels and six hourly temporal resolution, is used as initial and boundary conditions for the chemical
159 species (Buchholz et al., 2019). The meteorological forcing in CAM-Chem is driven by Modern-Era Retrospective
160 analysis for Research and Applications version 2 (MERRA2) reanalysis product (Emmons et al. 2020). Furthermore,
161 the Coupled Model Intercomparison Project round 6 (CMIP6) provides the anthropogenic aerosols within CAM-
162 Chem. The ERA5 (Hersbach et al., 2020), a most recent reanalysis product from European Centre for Medium range
163 Weather Forecasting (ECMWF), with 31 km spatial and hourly temporal resolution, was used to initialize the model
164 and as boundary conditions for the basic meteorological state parameters.

165 2.2 Experimental setup

166 According to the Department of Hydrology and Meteorology (DHM) of Nepal, the onset of the monsoon
167 occurred on June 14th, 2013, about a day after a normal onset date over eastern Nepal (DHM Nepal, 2022), and
168 generally, over the entire country within a week. Model simulations were performed for 31 days, from June 14th 00
169 UTC to July 15th 00 UTC, 2013. The mean precipitation over the Central Himalayan region (hereafter “CenHim”;



170 area indicated by the white-colored polygon in Fig. 1b) during the first month of the monsoon (31 days after the
171 monsoonal onset) from 2000-2021 is 11.84 mm/day with a standard deviation of 2.97 mm/day (see Fig. S1). For the
172 same period, the CenHim region in 2013 received 14.62 mm/day of precipitation which is within +1 standard
173 deviation of the climatology mean.

174 Two one-way nested domains with a horizontal resolution of 9 km and 3 km were set up (see Fig. 1). The
175 model was divided into 61 vertical layers with the 50 hPa model top. The 9 km parent domain with 179×221 grids
176 covered the central and northern/eastern India, Bangladesh, Bhutan, and TP. The 3 km nested domain with $273 \times$
177 321 grid points was designed to include the CenHim, Nepal (with Mount Everest), the areas of most anthropogenic
178 emission sources over the central IGP, and the immediate Himalayan plateau region of Tibet. The model
179 configuration with the physical parameterizations used in this study is listed in Table 1. The double moment
180 Morrison microphysics scheme simulates the number and mass mixing ratio of hydrometeors, including cloud
181 droplets, rain, ice, snow, and graupel (Morrison et al., 2009). Previous studies have reasonably implemented the
182 Morrison microphysics, RRTMG for radiation, and YSU for the boundary layer to simulate and study the aerosol-
183 cloud-precipitation interaction on a cloud-resolving scale (e.g., Kant et al., 2021; Wu et al., 2018). The convective
184 parametrization was turned off for the 3 km domain. This consideration assumes that the model explicitly resolves
185 convective eddies, hence the term cloud-resolving scale. The convection parameterization is linked to significant
186 sources of uncertainty in larger-scale models (Prein et al., 2015), and it is recommended to use a cloud-resolving
187 scale to assess the indirect effect of aerosols in a convective system (Grell et al., 2011; Archer-Nicholls et al., 2016).
188 Furthermore, such fine resolution is necessary to adequately address the altitudinal gradient in the steep mountains
189 with characteristic altitudes ranging from 60 to 8000 m ASL in about 200 km horizontal distance.

190 Three simulations were performed to assess the sensitivity of the model to aerosol effects. A baseline or
191 control simulation (hereafter "CTL") includes all the emissions (anthropogenic, biogenic, fire, and aerosols from
192 chemistry boundary conditions). CTL includes the aerosol-radiation interaction, indirect effect of aerosols, wet
193 scavenging, and dry deposition of aerosols. To isolate the direct effect of aerosol, the second simulation that
194 resembles the CTL simulation is performed, but by turning off aerosol-radiation feedback (hereafter "NoARI"). The
195 comparison between the CTL and NoARI enables the assessment of effect of aerosol-radiation interaction (ARI
196 effect; Wu et al., 2018). The third experiment resembles the CTL, but it is performed by multiplying the
197 anthropogenic aerosols from the boundary condition and emission inventory by a factor of 10% (hereafter
198 "CLEAN"). Reducing polluted aerosol concentration to a more pristine environment has been implemented
199 previously in studying the impact of aerosols on clouds and precipitation (e.g., Manoj et al., 2021; Fan et al., 2013,
200 2007). Since the CLEAN scenario is not entirely aerosol-free, the presence of the 10% anthropogenic aerosols and
201 contribution from the fire and biogenic emissions can influence the assessment of the ACI effect. So, we attempt to
202 broadly examine the microphysical effect of anthropogenic aerosols by comparing NoARI to CLEAN simulations
203 (ACI effect). For completeness and as an effort to assess the uncertainty of anthropogenic aerosol loading in the
204 region, a fourth simulation was performed using CTL but doubling aerosol concentration (D_AERO). Early results
205 in this study suggested that the CTL simulation predicted a relatively low AOD compared to remote sensing



206 retrievals. We use results and discuss the effect of the D_AERO simulations when necessary. Also, unless
207 mentioned, we examine and present the results using the analysis from the inner domain.

208 To examine the aerosol-precipitation elevational dependence, we divided the CenHim into 30 different bins
209 at an increasing interval of 200 m up to 6000 m and one bin for elevation above 6000 m above sea level (ASL).
210 Figure 2 shows the elevation distribution of the number of grid points in the CenHim and the corresponding mean
211 CTL precipitation. The relatively small number of grid points at higher elevations suggests a drop in the statistical
212 robustness of the analyses. When possible, we perform statistical significance tests using the student's t-test at the
213 90% confidence level to control for the statistical signal and noise. The maximum number of grid points (7113) is
214 present below 200 meters, while only 176 grid points are present above 6000 meters over the CenHim. The diurnal
215 variation and the elevational dependency of each variable are obtained by computing the average among all the grid
216 points within each bin of the elevational range.

217 **2.3 Model Evaluation**

218 CTL precipitation fields were evaluated using the sparsely distributed network of 90 rain gauge stations
219 measuring daily accumulations (measured at 03 UTC) and provided by the Department of Hydrology and
220 Meteorology, Nepal (see Fig. 1b). The altitudinal station distribution ranges from 60 to 2744 m ASL. The spatial
221 distribution of simulated precipitation was compared with the half-hourly Integrated Multi-satellite Retrievals for
222 Global Precipitation Measurement (IMERG) level-3 data at $0.1^\circ \times 0.1^\circ$ horizontal resolution (Huffman et al., 2019).

223 CTL simulated 550 nm Aerosol Optical Depth (AOD) is evaluated against the AOD retrievals from four
224 ground-based Aerosol Robotic Network (AERONET version 3 level 2.0; Kathmandu Bode, Pokhara, Kanpur, and
225 Jaipur; see Fig. 1a), satellite-based Moderate Resolution Imaging Spectroradiometer available at 10 km grid size
226 [MODIS Terra (MOD04_L2; sensed at 1030 LST) and Aqua (MYD04_L2; sensed at 1330 LST)], and MERRA2
227 reanalysis product (three hourly; $0.5^\circ \times 0.625^\circ$ spatial resolution). The spatial distribution of simulated AOD is
228 compared with MODIS (level 3; $1^\circ \times 1^\circ$) and MERRA2 reanalysis product (three hourly; $0.5^\circ \times 0.625^\circ$ spatial
229 resolution). The combined Dark Target and Deep Blue 550 nm AOD product from Terra and Aqua on-board
230 MODIS satellites are used for comparison. AERONET AOD data were obtained for 1000 to 1100 LST (± 30 minutes
231 of Terra overpass time) and 1300 to 1400 LST (± 30 minutes of Aqua overpass time) to match up the MODIS
232 overpass times. For time consistency, we used 1045 LST (0500 UTC) and 1345 LST (0800 UTC) as the nearest
233 simulated AOD times. The AERONET and MODIS retrievals of aerosol properties are limited during the
234 monsoonal season since they provide the AOD data measured in cloud-free conditions.

235 Since no upper air soundings are available in CenHim, radiosonde observations from the
236 <http://weather.uwyo.edu/upperair/sounding.html> at the Patna station, located south of CenHim, (25.60°N, 85.1°E, 60
237 m ASL, only available at 00 UTC; see Fig. 1a) was used to evaluate upper-air meteorological parameters
238 (temperature, zonal and meridional wind components, and mixing ratio). Sounding data was interpolated at 36
239 pressure levels between 100 and 975 hPa with an increment of 25 hPa.

240



241 3. Results and Discussion

242 3.1 Model Evaluation

243 Figure 3 shows the time series of the simulated AOD compared with the ground and satellited based AOD from
244 AERONET and MODIS Aqua and Terra. Though limited data points are available for comparison, the CTL
245 consistently underestimated the AOD, while D_AERO is comparable in magnitude with remotely sensed AOD (Fig.
246 3). Figure 4 shows the spatial distribution of mean MODIS, MERRA2, and simulated AOD during the simulation
247 period. Though the CTL underestimated the AOD in magnitude, it captured the spatial distribution of AOD
248 compared to the MODIS (Fig. 4a) and MERRA2 (Fig. 4b). Due to the higher emission rate, the aerosol is heavily
249 concentrated over the foothills and the IGP compared to the higher elevation of the mountainous terrain. The
250 variation in the AOD along with the topographical transect from lower to higher elevation is clearly illustrated in
251 Fig. 4. Not surprisingly, simulated AOD is lower for the CLEAN simulation over the entire domain, with the
252 differences being maximum in the lowlands (Fig. 4b). Although higher mountainous terrain is polluted compared to
253 the CLEAN scenario, the CTL AOD shows that it remains pristine compared to IGP due to the strong stratification
254 of aerosol emission with elevation and limited transport due to the topographical barrier. The doubling of the
255 anthropogenic aerosols in D_AERO resulted in increased AOD comparable to the MODIS and MERRA2 products
256 (Fig. 4d). It should be noted that the MODIS and MERRA2 are at coarser resolution and might have some biases
257 related to the scale differences.

258 Underestimation of AOD by WRF-Chem is a well-known model bias and has also been reported in the east
259 Asian monsoon region (Wu et al., 2013), Indian monsoon region (Soni et al., 2018; Govardhan et al., 2015), and
260 Indo Gangetic Plain during monsoon by around 50% (Sarangi et al., 2015). Also, Regional Climate Model
261 (RegCM4) underestimated AODs by a factor of 2 to 5 over south Asia in the period 2005 to 2007 (Nair et al., 2012).
262 Mues et al. (2018) showed that the EDGAR HTAP v2.2 implemented with WRF-Chem underestimates the black
263 carbon concentration over the Kathmandu valley by 80% in May of 2013, and one of the reasons might be the
264 underrepresentation of mobile emissions. The lower estimation of the aerosol emission over Nepal by the global
265 emission inventory is mainly due to the coarser resolution, emission factors, and lack of residential energy
266 consumption consideration (Sadavarte et al., 2019). Other limitations that might contribute to the lower estimation
267 of aerosol loading might be due to the different year used for emission inventory preparation (for 2010) and
268 simulation in this study, the lack of representation of secondary organic aerosols, and not accounting for all major
269 sources of emissions (e.g., emission due to infrastructure construction). Despite these well-known structural errors
270 that have been attributed to emissions inventory and potentially result in low biases in the impact of aerosols, our
271 results can provide meaningful insight into the role of aerosols in modulating the elevation dependence precipitation.

272



273 The mean temperature, mixing ratio, and zonal and meridional wind bias profiles from the simulated output
274 sampled from the upper air sounding observations at the Patna location are shown in Fig. S2. The model exhibits the
275 vertical easterly systematic bias between 950 and 300 hPa. Above 900hPa, a dry bias (significant above 575 hPa)
276 and northerly biases are present. The cool bias prevails below 775 hPa, while the warm bias is present in the mid-to-
277 upper troposphere. Though both the domains revealed a similar biases pattern, the cloud-resolving domain exhibited
278 smaller biases.

279 Figure 5 shows the error statistics of daily precipitation at different gauge stations and simulated precipitation at
280 the nearest grid point over Nepal. The biases in the simulated precipitation varied with elevation, where low-land
281 areas (< 500 m ASL) depicted the larger bias, while the altitude between 500 and 1500 m exhibited the smallest
282 bias. The mean bias estimation (MBE) across the rain gauge stations was lower by 0.29 mm/day with a mean root
283 mean square error (RMSE) of 27.52 mm/day. The daily mean accumulated precipitation from the model correlated
284 well (correlation coefficient of 0.5) with the gauge station data. The maximum mean correlation was observed for
285 the elevation between 500 and 1500 meters, the range of altitude that also depicted the minimum RMSE and MAE.
286 Though some over or underestimation of the precipitation and higher RMSE, there is a good agreement between the
287 onset and accumulated precipitation between the simulation and rain gauge stations (Fig. 5e-h). Also, as suggested
288 earlier, the lower concentration of aerosols can add up to the biases in the simulated precipitation. The manual
289 recording of the gauge station data and the under catch or losses due to wind speed/direction can add up to the
290 uncertainties in the precipitation data collection (Talchabhadel et al., 2017) and these model evaluation assessments.
291 Also, since most rain gauge stations are over the valley floor, the precipitation simulated over the mountain top
292 cannot be compared with the observational network.

293 Figure 6 shows the mean hourly precipitation estimates from IMERG, CTL, and the bias of CTL relative to the
294 IMERG estimation. Compared to IMERG, the model underestimated the precipitation amount over the IGP, while
295 the wet bias of the model is pronounced over the mountains of the CenHim. In general, though some biases in
296 precipitation exist, the model captured the overall feature of the precipitation distribution. The model reasonably
297 captured the elevational gradient of precipitation with lower precipitation over the lowlands, maximum mid-
298 mountainous precipitation associated with orographic forcing, and reduced leeward precipitation over northwestern
299 Nepal and the TP. The point precipitation pattern over the peaks of the mountain might be due to the strong
300 orographic lifting associated with the convective cells. The overestimation of the precipitation by the WRF-Chem
301 has also been reported in other studies over the Himalayan region (e.g., Barman and Gokhale, 2022; Sicard et al.,
302 2021; Adhikari and Mejia, 2022) and can be associated with the uncertainties from the physical parameterizations
303 (e.g., Baró et al., 2015; Zhang et al., 2021). However, note that the finer resolution simulation better resolves the
304 orographic forcing and can represent the precipitation over the complex terrain. Also, IMERG is at a coarser
305 resolution than the model, and some biases might be related to the scale differences. The underprediction of
306 accumulated precipitation by IMERG is evident over the rain gauge stations throughout the CenHim (Fig. 5e-h) and
307 is consistent with the (Sharma et al., 2020a). The pronounced differences over the higher terrains of CenHim can
308 also be associated with the underprediction of extreme precipitation events (> 25mm/day) by IMERG (Sharma et al.,



309 2020b), which might be related to the weak detection of shallow orographic forced precipitation event (Cao et al.,
310 2018; Arulraj and Barros, 2019; Shige and Kummerow, 2016).

311 **3.2 Aerosol Effect on Precipitation**

312 Figure 7 (a-c) shows the effect of aerosol on the spatial distribution of the mean hourly precipitation. Due to the total
313 effect of aerosols, precipitation increases over the elevation below 2000 m ASL except for the region just south of
314 Nepal, with a pronounced enhancement by the ACI effect. At the same time, the reduced precipitation occurred over
315 the high elevational region of the entire CenHim due to the total effect of aerosol. Figure 8a shows the diurnal
316 variation of precipitation as a function of terrain elevation. Minimum precipitation occurred throughout the
317 elevations during the late morning (0900 to 1200 local time). The mid-altitude range, especially between 1000 and
318 2000 m ASL, of CenHim experiences double peaks with stronger daytime and weaker nighttime precipitation (Fig.
319 8a). The averaging of the entire CenHim might influence the diurnal features of intraregional precipitation; however,
320 the diurnal pattern is consistent with the satellite-based findings of Fujinami et al. (2021). The surface heating and
321 the orographic forcing enhance the convergence of daytime upslope moisture flow resulting in higher daytime
322 precipitation over the southern slopes (Fujinami et al., 2021). In contrast, the adjacent foothills (below 600 m ASL)
323 are characterized by single midnight to early morning peak due to the convergence of stronger nocturnal jets with
324 the downslope winds (Fujinami et al., 2021; Terao et al., 2006). Precipitation over the higher elevation above 5000
325 m ASL and in the TP (not shown) is characterized by the afternoon peak and is consistent with Liu et al. (2022).

326 The diurnal variation of precipitation due to the aerosols effect as a function of elevation is presented
327 in Fig. 8 (b-d) and shows an inconsistent response to the anthropogenic aerosols along the elevational gradient.
328 Significant enhancement of precipitation occurred due to aerosols over the lower elevation (below 2000 m ASL)
329 from the early morning to noon. In contrast, the aerosol suppressed afternoon (1400 to 1800 local time) precipitation
330 over the lower elevation. The significant suppression of precipitation is observed over the higher terrain above 3000
331 m ASL during most of the day. Both the ARI and ACI effect of aerosols tend to reduce the precipitation over the
332 higher elevation above 3000 m ASL. The afternoon suppression of precipitation over the lowlands (below 2000 m
333 ASL) is dominated by the ARI effect (Fig. 8c). It is noteworthy that, though the ACI effect of aerosols suppressed
334 the nighttime (after 1800 LST) precipitation below 1000 m ASL, it extended the enhancement of precipitation to the
335 higher elevation up to 3600 m ASL (Fig. 8d). This can be attributed to the microphysical effect of aerosols delaying
336 the conversion of smaller cloud droplets to raindrops and enhancing the cloud lifetime, resulting in larger advection
337 time for orographic clouds, increasing the downwind precipitation (Givati and Rosenfeld, 2004; Choudhury et al.,
338 2019).

339 Variability in the amount of hourly precipitation increases from lower to higher altitudes (Fig. 2b), possibly
340 due to the orographic feature associated with the abrupt change in the topographical gradient. To further investigate
341 the response of elevational-dependent precipitation to the aerosols, we classified the mean precipitation intensity
342 into heavy (> 1.04 mm/hr), moderate (between 0.42 and 1.04 mm/hr), and light (< 0.42 mm/hr) precipitation regime.
343 A similar classification procedure has also been implemented by Sharma et al. (2020) for daily accumulated
344 precipitation over Nepal Himalayas and for hourly precipitation over eastern China by Shao et al. (2022). Figures



345 9 and 10 show the differences and relative change (%) in elevation dependence of the precipitation regime in
346 precipitation due to different effects of aerosols and reveal a contrasting elevational response. Though the ACI effect
347 slightly enhances the light precipitation below 1000 m ASL, the ARI effect dominates and monotonically suppresses
348 the mean light precipitation by 17% over the CenHim. Whereas the ACI effect enhances the precipitation below
349 3000 m ASL and shows a most prominent impact on moderate to heavy precipitation regimes. Contrasting to the
350 lower elevation, above 3000 m ASL, the ACI effect of aerosols suppressed all regimes of the precipitation intensity.
351 The elevation between 1000 and 3000 m ASL acts as the region below and above which the different intensity of
352 precipitation responds in the opposite direction to the effect of aerosols. The maximum increment (43%) in heavy
353 precipitation due to the aerosol effect occurred over the elevation bin between 200-400 m ASL (Fig. 10). Similarly,
354 the total precipitation was enhanced by 18% over the 200-400 m bin, while 5400-5600 m elevation experienced the
355 maximum reduction (21%). Below 2000 m ASL, due to the total effect of aerosols, the mean light precipitation is
356 suppressed by 19%, while moderate and heavy precipitation is enhanced by 3% and 12%, respectively. In contrast,
357 above 2000 m ASL, a significant suppression of all three categories of precipitation intensity is noticed with the
358 11% reduction in mean precipitation.

359 Other modeling studies over the mid-latitude mountains of the Great Alpine Region (Napoli et al., 2022)
360 and Sierra Nevada (Wu et al., 2018) also reported the suppression of precipitation in a polluted environment over the
361 higher elevation, consistent with our findings. However, contrasting to enhanced precipitation in our result, these
362 studies simulated the suppressed precipitation even in the lower elevations. This discrepancy might be associated
363 with the differences in the aerosol concentration from the heavily polluted upwind region of IGP, enhanced moisture
364 supply along with the monsoonal flow, and the steeper terrain of the Himalayas enhancing the orographic forcing
365 and convection compared to the Great Alpine and the Sierra Nevada.

366 In comparison to the CLEAN scenario, the elevational-dependent precipitation showed a similar response
367 in the diurnal cycle and spatial pattern to the increase in aerosols from CTL to D_AERO, besides the smaller
368 changes in the magnitude (not shown). The doubling in aerosols resulted in increased monthly mean heavy
369 precipitation below 2000 m ASL by 16% (4% higher compared to CTL run) and suppressed precipitation above the
370 2000 m ASL by 8% (similar to CTL run) compared to the CLEAN simulation. No significant differences were noted
371 in the change in light precipitation due to the doubling of aerosols. It might be related to the non-linear responses of
372 aerosol concentration to the convective intensity, microphysical, and dynamical effect (Fan et al., 2013; Chang et al.,
373 2015). Due to the stronger convection in the heavy precipitation regime, the potentiality of the aerosol getting
374 activated to cloud droplets increases in the presence of a higher aerosol concentration

375 **3.3 Aerosol Effect on Clouds**

376 Figure 11a shows the CTL simulated diurnal-elevation of cloud fraction over the CenHim and resembles
377 the diurnal precipitation pattern. The higher elevation above 4000 meters has lower cloud coverage throughout the
378 day due to the limited atmospheric moisture reaching the higher elevation. The ACI effect increases the cloud
379 fraction (over most of the elevation throughout the day due to the enhanced activation of aerosol as cloud droplets
380 (Fig. 11d). However, the ARI effect reduces the cloud coverage early in the morning below 2000 m ASL and the



381 suppression propagate higher in elevation during the afternoon and evening (Fig. 11c), which might be associated
382 with the weaker surface heating limiting the wind flows towards the slope of the mountain and afternoon orographic
383 cloud development. Although there is a noisier and a less consistent diurnal-elevation relationship, the total aerosol
384 effect is mostly that of enhancement of cloud cover. This result is consistent with long-term satellite retrieval of
385 cloudiness during high aerosol concentration days (Adhikari and Mejjia, 2021).

386 To further investigate the impact of anthropogenic aerosols on clouds and precipitation, the effect of
387 aerosols on vertical velocity, LWP, and IWP is performed by dividing the terrain elevation below and above 2000 m
388 ASL (Fig. 12), where the mean precipitation responded differently to the aerosols. Increased cloud coverage over the
389 CenHim due to the aerosol effect is associated with the ACI effect resulting in enhanced cloud liquid water path
390 (LWP) for all precipitation regimes (Fig. 12c-d). While ARI significantly contributes to the increase in ice water
391 path (IWP; by 10%) below 2000 m ASL (Fig. 12e) along with the settle but upward 5% increase in mean vertical
392 velocity (Fig. 12a). The ARI modulated increase in IWP below 2000 m ASL, where the amount of aerosol loading is
393 higher, can be attributed to the warming of the atmosphere resulting in the evaporation of droplets and contributing
394 to an increased upward moisture flux to the higher altitudes resulting in the formation of the ice. Other modeling
395 studies have also reported an increment in the cloud ice water content due to the radiative heating effect of biomass
396 burning (Liu et al., 2020) and dust aerosols (Dipu et al., 2013). While reduced IWP above 2000 m ASL due to ARI
397 might be dominated by the surface cooling effect suppressing the cloud development. The minimal ACI effect in
398 IWP is due to the lack of a model treating the activation of aerosol to ice nuclei.

399 The aerosol modulated vertical velocity below 2000 m ASL (Fig. 12a) suggests the convective strength is
400 suppressed/enhanced for the light/heavy precipitation regime. Additionally, due to the total aerosols effect, the
401 number of strong updraft events (mean vertical velocity higher than 0.5 ms^{-1}) increased by 10% below 2000 m ASL
402 (except for the lowest elevational bin below 200 m ASL) and reduced by 11% above 2000 m ASL (not shown).
403 Along with the stronger convection, the enhanced IWP and LWP indicate the invigoration of the cloud resulting in
404 increased heavier precipitation below 2000 m ASL. In contrast, the suppressed convection and more aerosol
405 activated as a higher number of smaller cloud droplets resulted in a nonprecipitating cloud suppressing the light
406 precipitation over the entire CenHim.

407 The suppression of light and enhanced heavy precipitation due to modulated convective strength by
408 anthropogenic aerosol is consistent with a simulated study over eastern China by Shao et al. (2022). The increased
409 precipitation over the foothills with an invigorated convection is consistent with our other study based on satellite
410 retrieval, showing an enhancement of precipitation due to the atmospheric aerosols over the southern slopes of the
411 Central Himalayas (Adhikari and Mejjia, 2021). Also, another satellite-based study by Choudhury et al. (2020)
412 suggests the higher aerosol loading with the increased moist static energy significantly contributed to the extreme
413 precipitation events over the Himalayan foothills. However, our results indicate the opposite response of
414 precipitation at different elevational bands to the increased aerosols. During the spring season, Barman and Gokhale
415 (2022) showed that the aerosol played a role in an increased influx of moisture over the lower terrain enhancing the
416 rainfall while limiting the moisture and suppressing the precipitation over the higher terrain of northeastern India.



417 3.4 Aerosol effect on Temperature and Radiation

418 Figure 13a shows the diurnal variation of decreasing temperature with increasing variability from low to
419 high elevations. The diurnal-elevation surface cooling effect due to anthropogenic aerosols during the daytime is
420 stronger throughout the elevational ranges (Fig. 13b-d). The daytime surface temperature cooling of $-1.3\text{ }^{\circ}\text{C}$ is likely
421 due to the total effect of aerosols over the terrain elevation above 4000 m ASL, with the ACI effect contributing to
422 most of the cooling ($-1.1\text{ }^{\circ}\text{C}$). The daytime variation of change in surface temperature is consistent with all sky
423 downwelling shortwave radiation flux at the surface (hereafter SW; Fig. 14). Over the Great Alpine Region of
424 Europe, Napoli et al. (2022) reported simulated results showing similar high-elevation daytime surface cooling
425 related to enhanced aerosol loadings. Another striking feature in Fig. 14 is the smaller but significant nighttime
426 surface temperature warming ($+0.03\text{ }^{\circ}\text{C}$) above 2000 m ASL, likely related to enhanced cloudiness (Fig. 11)
427 favoring trapping of the longwave radiation (Fig. S3). Our results indicate that the ACI effect of aerosols can
428 significantly contribute to nighttime warming over the higher elevation and contribute to warming by 0.08°C .

429 A prominent increase in minimum temperature in the recent decades over the higher elevation of the
430 Himalayan region has also been reported in previous studies (e.g., Dimri et al., 2022; Liu et al., 2009). The enhanced
431 nighttime minimum temperature has also been attributed to the enhanced cloud cover over the higher topographical
432 elevation (Rangwala and Miller, 2012; Liu et al., 2009) and increased cloud liquid water path due to the aerosol
433 indirect effect over East Asia (Huang et al., 2006b). Notably, the lack of aerosol snow interaction and deposition of
434 light-absorbing aerosols on the snow surfaces in our simulation can add uncertainties to simulated temperature
435 differences. The deposition of absorbing aerosol on snow has a crucial impact on the snow darkening effect, the
436 surface temperature, and the radiative forcing of the snowcapped Himalayan region (Qian et al., 2015; Sarangi et al.,
437 2019). Wu et al. (2018) showed that the inclusion of aerosol snow interaction in the model simulation resulted in a
438 significant increase in the surface temperature of the snowcapped mountain of Sierra Nevada.

439 Figure 14 (a-c) shows aerosol total, ARI, and ACI effects on the diurnal-elevational variation of all sky
440 SW, highlighting the stronger reduction of SW due to the aerosol effect at high elevations. The terrain elevation
441 above 4000 m ASL noted the reduction of SW by -82.8 W m^{-2} , and most contribution is from the ACI effect of
442 aerosols (Fig. 14c). The negative shortwave radiative perturbation at the surface due to the ACI effect is stronger
443 and can be attributed to the higher cloud liquid water path (LWP) and enhanced cloud albedo due to more aerosols
444 activated as condensation nuclei (Twomey, 1977). The stronger reduction of mid-day all sky SW over the higher
445 elevation compared to the lower elevation is due to the ACI effect, which results in the formation of persistent
446 polluted orographic clouds along with the upslope wind due to the ACI effect. A distinct difference in the impact of
447 an elevational gradient in the SW for the clear sky (excluding cloud; Fig. 14 d-f) and all sky (including cloud)
448 conditions are also noted. The reduction of the clear sky SW due to the aerosols at the terrain elevation below 1200
449 meters is stronger (-21 W m^{-2}), where the aerosol loadings are higher and is dominated by the ARI effect of aerosols.
450 The higher elevation above 4000 m ASL experienced the smaller negative perturbation of clear sky SW radiation ($>$
451 -5 W m^{-2}). This change in clear sky SW in a relatively polluted environment at a higher elevation is consistent with a
452 study by Marcq et al. (2010) reporting a similar change near the base camp (5079 m ASL) of Mount Everest.



453 The numerical simulation implemented in this study has several limitations. Due to the limited
454 computational resources, few sensitivity simulations were performed to assess the precipitation response to the
455 different effects of aerosols. Lack of complete effects of aerosols in the model, such as INP activation and formation
456 of secondary organic aerosols, can induce and add up the biases in our result. In this simulation, the contribution
457 from the impact of aerosol-surface-snow interaction is not included, which can also play a part in modulating the
458 mountain top surface temperature and orographic precipitation (Wu et al., 2018). The SNICAR (Snow, Ice, and
459 Aerosol Radiation) model (Flanner et al., 2007), capable of simulating the snow surface albedo and aerosol radiative
460 effect in snow, can be coupled with the WRF-Chem to study the aerosol-snow-interaction (Zhao et al., 2014). Also,
461 it is noted that there are biases in assessing the ACI effect associated with the presence of 10% aerosols and
462 contribution from the fire and biogenic emissions in the CLEAN scenario. Furthermore, the 3 km grid sizes might be
463 relatively coarser to resolve the orographic forcing and mountain-valley circulation of the steep and complex
464 topography of the Himalayas. Due to the inhomogeneity in the aerosol distribution over the complex topography,
465 improved emission inventory with diurnal distribution will help advance the current understanding of the diurnal
466 impact of aerosols on temperature distribution and the convective/precipitation process. There is a need for
467 continuous data collection from a denser distribution of observational networks (e.g., AERONET and weather
468 stations) with more meteorological variables along the elevational transect of the Himalayan topography, especially
469 over the high elevation region. It not only quantifies the long-term trend and pattern of the sensitive regions but also
470 helps evaluate and constrain numerical modeling studies in complex terrain.

471 **4 Conclusions**

472 The presence of steep mountainous terrain and orographic distribution drives the very complex and non-
473 linear precipitation system over the Central Himalayan region. Despite the importance of the hydrological processes
474 of the Himalayas, research studying the impact of aerosols in modulating the elevation-dependent precipitation over
475 the Central Himalayas using cloud-resolving numerical simulation has not been performed until now.

476 The first monsoonal month of 2013 (June 14 to July 15) is simulated using a high-resolution cloud-
477 resolving WRF-Chem numerical modeling to understand the impact of aerosols on the elevation-dependent
478 precipitation over the very complex terrain of the Central Himalayan region. In addition to explicitly resolving the
479 cloud evolution, the detailed topographical representation by the cloud-resolving scale model better simulates the
480 emission and transport processes of aerosols. So, the cloud-resolving simulation is important to provide better
481 insight and quantify the impact of aerosol on elevation-dependent precipitation over complex terrain. In addition to
482 CTL (baseline) simulation, two different numerical experiments were performed, similar to the CTL run but turning
483 off the aerosol radiation feedback and reducing the anthropogenic aerosols to 10% of CTL. The comparison between
484 the simulation experiments allowed us to assess and discuss the relative impact of aerosol radiation and cloud
485 interaction on the diurnal variation and different regimes of elevation-dependent precipitation and temperature.

486 Figure 15 illustrates the summaries of our main conclusions. We showed that the total effect of
487 anthropogenic aerosols cooled the daytime surface monotonically from lower to higher elevations. The higher
488 elevation showed a strong diurnal variation in surface temperature, with a strong cooling above 4000 m ASL during



489 the daytime (by -1.3°C) and above 2000m ASL, nighttime warming ($+0.03^{\circ}\text{C}$). The increased LWP and cloud
490 coverage during daytime with higher aerosol concentration is attributed to the reduced SW and daytime temperature,
491 while nighttime warming is due to the trapping of longwave radiation.

492 Our modeling experiment showed an altitudinal differential response by precipitation (intensity and diurnal
493 variation) to the anthropogenic aerosols. The mid elevation range, generally between 1000 and 3000 m ASL, act as a
494 transition layer where the diurnal variation and various intensity of precipitation respond differently to the ARI,
495 ACI, and total effect of aerosols. The total effect of aerosols tends to enhance the precipitation below 2000 m ASL,
496 while a significant reduction of precipitation occurs above 2000 m ASL with a dominating contribution from the
497 ACI effect. The total effect of aerosols reduced the mean light precipitation by 17%. However, along with the
498 stronger convection below 2000 m ASL the ACI effect dominated and resulted in the enhancement of the heavy
499 precipitation by 12%, contrasting to the reduction by 8% over the higher elevations. The result of our study can have
500 a broader impact and suggests that enhanced heavy precipitation over the elevation below 2000 m ASL can increase
501 the risk for extreme events (floods and landslides), while the suppressed high elevation precipitation can be critical
502 for the regional supply of water resources (Immerzeel et al., 2010). Despite some biases and existing uncertainties in
503 the model, our results underline the noticeable impact of aerosols on elevational-dependent precipitation. Though we
504 simulated only the first month of the monsoon, our results indicate that the anthropogenic aerosol plays a significant
505 role in enhancing (suppressing) the low elevation (high elevation) precipitation. The underlying aerosol-
506 precipitation-elevation relationships may vary during different states of the monsoon as the abundance of aerosols
507 tends to decrease during the mature to demise stage of the monsoon. Hence, longer term simulations with a complete
508 parametrization scheme to include the ice phase aerosol-cloud interaction and aerosol-snow interaction pathways
509 and better emission inventory with characterization are warranted to deepen our understanding of such elevational
510 dependence. This could be the future scope and extension of this study.

511



512 **Data Availability**

513 The MODIS data are available through the following link: <https://ladsweb.modaps.eosdis.nasa.gov/search/order> The
514 IMERG data are available through the following link: <https://disc.gsfc.nasa.gov/>
515 The DHM rain gauge station precipitation data can be requested through the following link:
516 <https://www.dhm.gov.np/request-data>
517 The upper air sounding data are available through the following link:
518 <http://weather.uwyo.edu/upperair/sounding.html>
519 The AERONET data are available through the following link: https://aeronet.gsfc.nasa.gov/cgi-bin/webtool_aod_v3
520

521 **Author contribution**

522 PA and JM designed the numerical experiments, and PA performed the simulations. PA and JM performed the
523 analysis and interpreted the results. PA prepared the original draft of the manuscript with equal contributions from
524 JM.

525

526 **Competing interests**

527 The authors declare that they have no conflict of interest.

528

529 **Acknowledgements**

530 The authors would like to thank the Division of Atmospheric Sciences, Desert Research Institute (DRI), and the
531 University of Nevada Reno for supporting this research. The Division of Atmospheric Sciences partially funds Dr.
532 Mejia at DRI. We also thank the assistantship support for Mr. Adhikari from the DRI and through Dr. Mejia's DRI
533 Institute Project Assignment funds. We would like to acknowledge high-performance computing support from
534 Cheyenne (doi:10.5065/D6RX99HX) provided by NCAR's Computational and Information Systems Laboratory,
535 sponsored by the National Science Foundation. We also thank NASA for providing the IMERG, AERONET, and
536 MERRA2 data. We also thank the Department of Hydrology and Meteorology Nepal for providing the precipitation
537 data from the rain gauge stations. We would like to acknowledge Dr. Douglas Lowe (University of Manchester) and
538 the Atmospheric Chemistry Observations and Modeling Lab (ACOM) of NCAR for providing the WRF-Chem
539 preprocessor tool.

540

541



542 References

- 543 Abdul-Razzak, H. and Ghan, S. J.: A parameterization of aerosol activation 3. Sectional representation, *Journal of*
544 *Geophysical Research: Atmospheres*, 107, AAC 1-1-AAC 1-6, <https://doi.org/10.1029/2001JD000483>, 2002.
- 545 Ackerman, A. S., Toon, O. B., Stevens, D. E., Heymsfield, A. J., Ramanathan, V., and Welton, E. J.: Reduction of
546 Tropical Cloudiness by Soot, *Science*, <https://doi.org/10.1126/science.288.5468.1042>, 2000.
- 547 Adhikari, P. and Mejjia, J. F.: Influence of aerosols on clouds, precipitation and freezing level height over the
548 foothills of the Himalayas during the Indian summer monsoon, *Clim Dyn*, [https://doi.org/10.1007/s00382-021-](https://doi.org/10.1007/s00382-021-05710-2)
549 05710-2, 2021.
- 550 Adhikari, P. and Mejjia, J. F.: Impact of transported dust aerosols on precipitation over the Nepal Himalayas using
551 convection-permitting WRF-Chem simulation, *Atmospheric Environment: X*, 15, 100179,
552 <https://doi.org/10.1016/j.aeaoa.2022.100179>, 2022.
- 553 Albrecht, B. A.: Aerosols, Cloud Microphysics, and Fractional Cloudiness, *Science*, 245, 1227–1230,
554 <https://doi.org/10.1126/science.245.4923.1227>, 1989.
- 555 Andreae, M. O. and Rosenfeld, D.: Aerosol–cloud–precipitation interactions. Part 1. The nature and sources of
556 cloud-active aerosols, *Earth-Science Reviews*, 89, 13–41, <https://doi.org/10.1016/j.earscirev.2008.03.001>, 2008.
- 557 Andreae, M. O., Rosenfeld, D., Artaxo, P., Costa, A. A., Frank, G. P., Longo, K. M., and Silva-Dias, M. A. F.:
558 Smoking rain clouds over the Amazon, *Science*, 303, 1337–1342, <https://doi.org/10.1126/science.1092779>, 2004.
- 559 Archer-Nicholls, S., Lowe, D., Schultz, D. M., and McFiggans, G.: Aerosol–radiation–cloud interactions in a
560 regional coupled model: the effects of convective parameterisation and resolution, *Atmos. Chem. Phys.*, 16, 5573–
561 5594, <https://doi.org/10.5194/acp-16-5573-2016>, 2016.
- 562 Arulraj, M. and Barros, A. P.: Improving quantitative precipitation estimates in mountainous regions by modelling
563 low-level seeder-feeder interactions constrained by Global Precipitation Measurement Dual-frequency Precipitation
564 Radar measurements, *Remote Sensing of Environment*, 231, 111213, <https://doi.org/10.1016/j.rse.2019.111213>,
565 2019.
- 566 Barman, N. and Gokhale, S.: Aerosol influence on the pre-monsoon rainfall mechanisms over North-East India: A
567 WRF-Chem study, *Atmospheric Research*, 268, 106002, <https://doi.org/10.1016/j.atmosres.2021.106002>, 2022.
- 568 Baró, R., Jiménez-Guerrero, P., Balzarini, A., Curci, G., Forkel, R., Grell, G., Hirtl, M., Honzak, L., Langer, M.,
569 Pérez, J. L., Pirovano, G., San José, R., Tuccella, P., Werhahn, J., and Žabkar, R.: Sensitivity analysis of the
570 microphysics scheme in WRF-Chem contributions to AQMEII phase 2, *Atmospheric Environment*, 115, 620–629,
571 <https://doi.org/10.1016/j.atmosenv.2015.01.047>, 2015.
- 572 Bradley, R. S., Keimig, F. T., Diaz, H. F., and Hardy, D. R.: Recent changes in freezing level heights in the Tropics
573 with implications for the deglaciation of high mountain regions, *Geophysical Research Letters*, 36,
574 <https://doi.org/10.1029/2009GL037712>, 2009.
- 575 Buchholz, R. R., Emmons, L. K., Tilmes, S., and The CESM2 Development Team: CESM2. 1/CAM-chem
576 instantaneous output for boundary conditions, UCAR/NCAR-Atmospheric Chemistry Observations and Modeling
577 Laboratory, <https://doi.org/10.5065/NMP7-EP60>, 2019.
- 578 Cao, Q., Painter, T. H., Currier, W. R., Lundquist, J. D., and Lettenmaier, D. P.: Estimation of Precipitation over the
579 OLYMPEX Domain during Winter 2015/16, *Journal of Hydrometeorology*, 19, 143–160,
580 <https://doi.org/10.1175/JHM-D-17-0076.1>, 2018.



- 581 Chang, D., Cheng, Y., Reutter, P., Trentmann, J., Burrows, S. M., Spichtinger, P., Nordmann, S., Andreae, M. O.,
582 Pöschl, U., and Su, H.: Comprehensive mapping and characteristic regimes of aerosol effects on the formation and
583 evolution of pyro-convective clouds, *Atmospheric Chemistry and Physics*, 15, 10325–10348,
584 <https://doi.org/10.5194/acp-15-10325-2015>, 2015.
- 585 Chapman, E. G., Jr, W. I. G., Easter, R. C., Barnard, J. C., Ghan, S. J., Pekour, M. S., and Fast, J. D.: Coupling
586 aerosol-cloud-radiative processes in the WRF-Chem model: Investigating the radiative impact of elevated point
587 sources, *Atmos. Chem. Phys.*, 20, 2009.
- 588 Cho, C., Li, R., Wang, S.-Y., Yoon, J.-H., and Gillies, R. R.: Anthropogenic footprint of climate change in the June
589 2013 northern India flood, *Clim Dyn*, 46, 797–805, <https://doi.org/10.1007/s00382-015-2613-2>, 2016.
- 590 Choudhury, G., Tyagi, B., Singh, J., Sarangi, C., and Tripathi, S. N.: Aerosol-orography-precipitation – A critical
591 assessment, *Atmospheric Environment*, 214, 116831, <https://doi.org/10.1016/j.atmosenv.2019.116831>, 2019.
- 592 Choudhury, G., Tyagi, B., Vissa, N. K., Singh, J., Sarangi, C., Tripathi, S. N., and Tesche, M.: Aerosol-enhanced
593 high precipitation events near the Himalayan foothills, *Atmospheric Chemistry and Physics*, 20, 15389–15399,
594 <https://doi.org/10.5194/acp-20-15389-2020>, 2020.
- 595 Dey, S. and Di Girolamo, L.: A decade of change in aerosol properties over the Indian subcontinent, *Geophysical
596 Research Letters*, 38, <https://doi.org/10.1029/2011GL048153>, 2011.
- 597 DHM Nepal: Monsoon onset and withdrawal date information.
598 http://www.dhm.gov.np/uploads/climatic/841739888monsoon%20onset%20n%20withdrawal%20English_6%20June%202022.pdf, 2022.
599
- 600 Dimri, A. P., Palazzi, E., and Daloz, A. S.: Elevation dependent precipitation and temperature changes over Indian
601 Himalayan region, *Clim Dyn*, <https://doi.org/10.1007/s00382-021-06113-z>, 2022.
- 602 Dipu, S., Prabha, T. V., Pandithurai, G., Dudhia, J., Pfister, G., Rajesh, K., and Goswami, B. N.: Impact of elevated
603 aerosol layer on the cloud microphysical properties prior to monsoon onset, *Atmospheric Environment*, 70, 454–
604 467, <https://doi.org/10.1016/j.atmosenv.2012.12.036>, 2013.
- 605 Eidhammer, T., Barth, M. C., Petters, M. D., Wiedinmyer, C., and Prenni, A. J.: Aerosol microphysical impact on
606 summertime convective precipitation in the Rocky Mountain region, *Journal of Geophysical Research:
607 Atmospheres*, 119, 11,709–11,728, <https://doi.org/10.1002/2014JD021883>, 2014.
- 608 Emmons, L. K., Schwantes, R. H., Orlando, J. J., Tyndall, G., Kinnison, D., Lamarque, J.-F., Marsh, D., Mills, M.
609 J., Tilmes, S., Bardeen, C., Buchholz, R. R., Conley, A., Gettelman, A., Garcia, R., Simpson, I., Blake, D. R.,
610 Meinardi, S., and Pétron, G.: The Chemistry Mechanism in the Community Earth System Model Version 2
611 (CESM2), *Journal of Advances in Modeling Earth Systems*, 12, e2019MS001882,
612 <https://doi.org/10.1029/2019MS001882>, 2020.
- 613 Fan, J., Zhang, R., Li, G., and Tao, W.-K.: Effects of aerosols and relative humidity on cumulus clouds, *Journal of
614 Geophysical Research: Atmospheres*, 112, <https://doi.org/10.1029/2006JD008136>, 2007.
- 615 Fan, J., Leung, L. R., Rosenfeld, D., Chen, Q., Li, Z., Zhang, J., and Yan, H.: Microphysical effects determine
616 macrophysical response for aerosol impacts on deep convective clouds, *PNAS*, 110, E4581–E4590,
617 <https://doi.org/10.1073/pnas.1316830110>, 2013.
- 618 Fan, J., Rosenfeld, D., Yang, Y., Zhao, C., Leung, L. R., and Li, Z.: Substantial contribution of anthropogenic air
619 pollution to catastrophic floods in Southwest China, *Geophysical Research Letters*, 42, 6066–6075,
620 <https://doi.org/10.1002/2015GL064479>, 2015.



- 621 Fan, J., Leung, L. R., Rosenfeld, D., and DeMott, P. J.: Effects of cloud condensation nuclei and ice nucleating
622 particles on precipitation processes and supercooled liquid in mixed-phase orographic clouds, *Atmospheric*
623 *Chemistry and Physics*, 17, 1017–1035, <https://doi.org/10.5194/acp-17-1017-2017>, 2017.
- 624 Fast, J. D., Gustafson, W. I., Easter, R. C., Zaveri, R. A., Barnard, J. C., Chapman, E. G., Grell, G. A., and Peckham,
625 S. E.: Evolution of ozone, particulates, and aerosol direct radiative forcing in the vicinity of Houston using a fully
626 coupled meteorology-chemistry-aerosol model, *Journal of Geophysical Research: Atmospheres*, 111,
627 <https://doi.org/10.1029/2005JD006721>, 2006.
- 628 Flanner, M. G., Zender, C. S., Randerson, J. T., and Rasch, P. J.: Present-day climate forcing and response from
629 black carbon in snow, *Journal of Geophysical Research: Atmospheres*, 112, <https://doi.org/10.1029/2006JD008003>,
630 2007.
- 631 Fujinami, H., Fujita, K., Takahashi, N., Sato, T., Kanamori, H., Sunako, S., and Kayastha, R. B.: Twice-Daily
632 Monsoon Precipitation Maxima in the Himalayas Driven by Land Surface Effects, *Journal of Geophysical Research:*
633 *Atmospheres*, 126, e2020JD034255, <https://doi.org/10.1029/2020JD034255>, 2021.
- 634 Gery, M. W., Whitten, G. Z., Killus, J. P., and Dodge, M. C.: A photochemical kinetics mechanism for urban and
635 regional scale computer modeling, *Journal of Geophysical Research: Atmospheres*, 94, 12925–12956,
636 <https://doi.org/10.1029/JD094iD10p12925>, 1989.
- 637 Ghimire, S., Choudhary, A., and Dimri, A. P.: Assessment of the performance of CORDEX-South Asia experiments
638 for monsoonal precipitation over the Himalayan region during present climate: part I, *Clim Dyn*, 50, 2311–2334,
639 <https://doi.org/10.1007/s00382-015-2747-2>, 2018.
- 640 Givati, A. and Rosenfeld, D.: Quantifying Precipitation Suppression Due to Air Pollution, *Journal of Applied*
641 *Meteorology and Climatology*, 43, 1038–1056, [https://doi.org/10.1175/1520-0450\(2004\)043<1038:QPSDTA>2.0.CO;2](https://doi.org/10.1175/1520-0450(2004)043<1038:QPSDTA>2.0.CO;2), 2004.
- 643 Govardhan, G., Nanjundiah, R. S., Satheesh, S. K., Krishnamoorthy, K., and Kotamarthi, V. R.: Performance of
644 WRF-Chem over Indian region: Comparison with measurements, *J Earth Syst Sci*, 124, 875–896,
645 <https://doi.org/10.1007/s12040-015-0576-7>, 2015.
- 646 Grell, G., Freitas, S. R., Stuefer, M., and Fast, J.: Inclusion of biomass burning in WRF-Chem: impact of wildfires
647 on weather forecasts, *Atmospheric Chemistry and Physics*, 11, 5289–5303, [https://doi.org/10.5194/acp-11-5289-](https://doi.org/10.5194/acp-11-5289-2011)
648 2011, 2011.
- 649 Grell, G. A. and Dévényi, D.: A generalized approach to parameterizing convection combining ensemble and data
650 assimilation techniques, *Geophysical Research Letters*, 29, 38-1-38–4, <https://doi.org/10.1029/2002GL015311>,
651 2002.
- 652 Grell, G. A., Peckham, S. E., Schmitz, R., McKeen, S. A., Frost, G., Skamarock, W. C., and Eder, B.: Fully coupled
653 “online” chemistry within the WRF model, *Atmospheric Environment*, 39, 6957–6975,
654 <https://doi.org/10.1016/j.atmosenv.2005.04.027>, 2005.
- 655 Guenther, A., Karl, T., Harley, P., Wiedinmyer, C., Palmer, P. I., and Geron, C.: Estimates of global terrestrial
656 isoprene emissions using MEGAN (Model of Emissions of Gases and Aerosols from Nature), *Atmospheric*
657 *Chemistry and Physics*, 6, 3181–3210, <https://doi.org/10.5194/acp-6-3181-2006>, 2006.
- 658 Guenther, A. B., Jiang, X., Heald, C. L., Sakulyanontvittaya, T., Duhl, T., Emmons, L. K., and Wang, X.: The
659 Model of Emissions of Gases and Aerosols from Nature version 2.1 (MEGAN2.1): an extended and updated
660 framework for modeling biogenic emissions, *Geoscientific Model Development*, 5, 1471–1492,
661 <https://doi.org/10.5194/gmd-5-1471-2012>, 2012.



- 662 Hallquist, M., Wenger, J. C., Baltensperger, U., Rudich, Y., Simpson, D., Claeys, M., Dommen, J., Donahue, N. M.,
663 George, C., Goldstein, A. H., Hamilton, J. F., Herrmann, H., Hoffmann, T., Iinuma, Y., Jang, M., Jenkin, M. E.,
664 Jimenez, J. L., Kiendler-Scharr, A., Maenhaut, W., McFiggans, G., Mentel, T. F., Monod, A., Prévôt, A. S. H.,
665 Seinfeld, J. H., Surratt, J. D., Szmigielski, R., and Wildt, J.: The formation, properties and impact of secondary
666 organic aerosol: current and emerging issues, *Atmospheric Chemistry and Physics*, 9, 5155–5236,
667 <https://doi.org/10.5194/acp-9-5155-2009>, 2009.
- 668 Hansen, J., Sato, M., and Ruedy, R.: Radiative forcing and climate response, *Journal of Geophysical Research:*
669 *Atmospheres*, 102, 6831–6864, <https://doi.org/10.1029/96JD03436>, 1997.
- 670 Haywood, J. and Boucher, O.: Estimates of the direct and indirect radiative forcing due to tropospheric aerosols: A
671 review, *Reviews of Geophysics*, 38, 513–543, <https://doi.org/10.1029/1999RG000078>, 2000.
- 672 Hersbach, H., Bell, B., Berrisford, P., Hirahara, S., Horányi, A., Muñoz-Sabater, J., Nicolas, J., Peubey, C., Radu,
673 R., Schepers, D., Simmons, A., Soci, C., Abdalla, S., Abellan, X., Balsamo, G., Bechtold, P., Biavati, G., Bidlot, J.,
674 Bonavita, M., De Chiara, G., Dahlgren, P., Dee, D., Diamantakis, M., Dragani, R., Flemming, J., Forbes, R.,
675 Fuentes, M., Geer, A., Haimberger, L., Healy, S., Hogan, R. J., Hólm, E., Janisková, M., Keeley, S., Laloyaux, P.,
676 Lopez, P., Lupu, C., Radnoti, G., de Rosnay, P., Rozum, I., Vamborg, F., Villaume, S., and Thépaut, J.-N.: The
677 ERA5 global reanalysis, *Quarterly Journal of the Royal Meteorological Society*, 146, 1999–2049,
678 <https://doi.org/10.1002/qj.3803>, 2020.
- 679 Hong, S.-Y., Noh, Y., and Dudhia, J.: A New Vertical Diffusion Package with an Explicit Treatment of Entrainment
680 Processes, *Mon. Wea. Rev.*, 134, 2318–2341, <https://doi.org/10.1175/MWR3199.1>, 2006.
- 681 Huang, J., Lin, B., Minnis, P., Wang, T., Wang, X., Hu, Y., Yi, Y., and Ayers, J. K.: Satellite-based assessment of
682 possible dust aerosols semi-direct effect on cloud water path over East Asia, *Geophysical Research Letters*, 33,
683 <https://doi.org/10.1029/2006GL026561>, 2006a.
- 684 Huang, Y., Dickinson, R. E., and Chameides, W. L.: Impact of aerosol indirect effect on surface temperature over
685 East Asia, *Proceedings of the National Academy of Sciences*, 103, 4371–4376,
686 <https://doi.org/10.1073/pnas.0504428103>, 2006b.
- 687 Huffman, G. J., Stocker, E. F., Bolvin, D. T., Nelkin, E. J., and Tan, J.: GPM IMERG Early Precipitation L3 Half
688 Hourly 0.1 degree x 0.1 degree V06, Goddard Earth Sciences Data and Information Services Center (GES DISC),
689 Greenbelt, MD, <https://doi.org/10.5067/GPM/IMERG/3B-HH-E/06>, 2019.
- 690 Iacono, M. J., Delamere, J. S., Mlawer, E. J., Shephard, M. W., Clough, S. A., and Collins, W. D.: Radiative forcing
691 by long-lived greenhouse gases: Calculations with the AER radiative transfer models, *Journal of Geophysical*
692 *Research: Atmospheres*, 113, <https://doi.org/10.1029/2008JD009944>, 2008.
- 693 Immerzeel, W. W., van Beek, L. P. H., and Bierkens, M. F. P.: Climate Change Will Affect the Asian Water
694 Towers, *Science*, 328, 1382–1385, <https://doi.org/10.1126/science.1183188>, 2010.
- 695 IPCC: Climate change 2013: The Physical Science Basis: Working Group I Contribution to the Fifth Assessment
696 Report of the Intergovernmental Panel on Climate, Cambridge University Press, 1553 pp., 2013.
- 697 Janssens-Maenhout, G., Crippa, M., Guizzardi, D., Dentener, F., Muntean, M., Pouliot, G., Keating, T., Zhang, Q.,
698 Kurokawa, J., Wankmüller, R., Denier van der Gon, H., Kuenen, J. J. P., Klimont, Z., Frost, G., Darras, S., Koffi,
699 B., and Li, M.: HTAP_v2.2: a mosaic of regional and global emission grid maps for 2008 and 2010 to study
700 hemispheric transport of air pollution, *Atmospheric Chemistry and Physics*, 15, 11411–11432,
701 <https://doi.org/10.5194/acp-15-11411-2015>, 2015.
- 702 Ji, Z., Kang, S., Cong, Z., Zhang, Q., and Yao, T.: Simulation of carbonaceous aerosols over the Third Pole and
703 adjacent regions: distribution, transportation, deposition, and climatic effects, *Clim Dyn*, 45, 2831–2846,
704 <https://doi.org/10.1007/s00382-015-2509-1>, 2015.



- 705 Kang, S., Zhang, Q., Qian, Y., Ji, Z., Li, C., Cong, Z., Zhang, Y., Guo, J., Du, W., Huang, J., You, Q., Panday, A.
706 K., Rupakheti, M., Chen, D., Gustafsson, Ö., Thiemens, M. H., and Qin, D.: Linking atmospheric pollution to
707 cryospheric change in the Third Pole region: current progress and future prospects, *Natl Sci Rev*, 6, 796–809,
708 <https://doi.org/10.1093/nsr/nwz031>, 2019.
- 709 Kant, S., Panda, J., Rao, P., Sarangi, C., and Ghude, S. D.: Study of aerosol-cloud-precipitation-meteorology
710 interaction during a distinct weather event over the Indian region using WRF-Chem, *Atmospheric Research*, 247,
711 105144, <https://doi.org/10.1016/j.atmosres.2020.105144>, 2021.
- 712 Kaul, D. S., Gupta, T., Tripathi, S. N., Tare, V., and Collett, J. L.: Secondary Organic Aerosol: A Comparison
713 between Foggy and Nonfoggy Days, *Environ. Sci. Technol.*, 45, 7307–7313, <https://doi.org/10.1021/es201081d>,
714 2011.
- 715 Khain, A., Lynn, B., and Shpund, J.: High resolution WRF simulations of Hurricane Irene: Sensitivity to aerosols
716 and choice of microphysical schemes, *Atmospheric Research*, 167, 129–145,
717 <https://doi.org/10.1016/j.atmosres.2015.07.014>, 2016.
- 718 Koren, I., Kaufman, Y. J., Rosenfeld, D., Remer, L. A., and Rudich, Y.: Aerosol invigoration and restructuring of
719 Atlantic convective clouds, *Geophysical Research Letters*, 32, <https://doi.org/10.1029/2005GL023187>, 2005.
- 720 Kumar, M., Parmar, K. S., Kumar, D. B., Mhawish, A., Broday, D. M., Mall, R. K., and Banerjee, T.: Long-term
721 aerosol climatology over Indo-Gangetic Plain: Trend, prediction and potential source fields, *Atmospheric
722 Environment*, 180, 37–50, <https://doi.org/10.1016/j.atmosenv.2018.02.027>, 2018.
- 723 Lau, K. M., Kim, M. K., and Kim, K. M.: Asian summer monsoon anomalies induced by aerosol direct forcing: the
724 role of the Tibetan Plateau, *Clim Dyn*, 26, 855–864, <https://doi.org/10.1007/s00382-006-0114-z>, 2006.
- 725 Lau, W. K. M., Kim, K.-M., Shi, J.-J., Matsui, T., Chin, M., Tan, Q., Peters-Lidard, C., and Tao, W. K.: Impacts of
726 aerosol–monsoon interaction on rainfall and circulation over Northern India and the Himalaya Foothills, *Clim Dyn*,
727 49, 1945–1960, <https://doi.org/10.1007/s00382-016-3430-y>, 2017.
- 728 Li, Z., Lau, W. K.-M., Ramanathan, V., Wu, G., Ding, Y., Manoj, M. G., Liu, J., Qian, Y., Li, J., Zhou, T., Fan, J.,
729 Rosenfeld, D., Ming, Y., Wang, Y., Huang, J., Wang, B., Xu, X., Lee, S.-S., Cribb, M., Zhang, F., Yang, X., Zhao,
730 C., Takemura, T., Wang, K., Xia, X., Yin, Y., Zhang, H., Guo, J., Zhai, P. M., Sugimoto, N., Babu, S. S., and
731 Brasseur, G. P.: Aerosol and monsoon climate interactions over Asia, *Reviews of Geophysics*, 54, 866–929,
732 <https://doi.org/10.1002/2015RG000500>, 2016.
- 733 Liu, L., Cheng, Y., Wang, S., Wei, C., Pöhlker, M. L., Pöhlker, C., Artaxo, P., Shrivastava, M., Andreae, M. O.,
734 Pöschl, U., and Su, H.: Impact of biomass burning aerosols on radiation, clouds, and precipitation over the Amazon:
735 relative importance of aerosol–cloud and aerosol–radiation interactions, *Atmospheric Chemistry and Physics*, 20,
736 13283–13301, <https://doi.org/10.5194/acp-20-13283-2020>, 2020.
- 737 Liu, X., Cheng, Z., Yan, L., and Yin, Z.-Y.: Elevation dependency of recent and future minimum surface air
738 temperature trends in the Tibetan Plateau and its surroundings, *Global and Planetary Change*, 68, 164–174,
739 <https://doi.org/10.1016/j.gloplacha.2009.03.017>, 2009.
- 740 Liu, Z., Gao, Y., and Zhang, G.: How well can a convection-permitting-modelling improve the simulation of
741 summer precipitation diurnal cycle over the Tibetan Plateau?, *Clim Dyn*, 58, 3121–3138,
742 <https://doi.org/10.1007/s00382-021-06090-3>, 2022.
- 743 Lynn, E., Cuthbertson, A., He, M., Vasquez, J. P., Anderson, M. L., Coombe, P., Abatzoglou, J. T., and Hatchett, B.
744 J.: Technical note: Precipitation-phase partitioning at landscape scales to regional scales, *Hydrology and Earth
745 System Sciences*, 24, 5317–5328, <https://doi.org/10.5194/hess-24-5317-2020>, 2020.



- 746 Mahowald, N., Ward, D. S., Kloster, S., Flanner, M. G., Heald, C. L., Heavens, N. G., Hess, P. G., Lamarque, J.-F.,
747 and Chuang, P. Y.: Aerosol Impacts on Climate and Biogeochemistry, *Annual Review of Environment and*
748 *Resources*, 36, 45–74, <https://doi.org/10.1146/annurev-environ-042009-094507>, 2011.
- 749 Manoj, M. G., Lee, S.-S., and Li, Z.: Competing aerosol effects in triggering deep convection over the Indian
750 Region, *Clim Dyn*, 56, 1815–1835, <https://doi.org/10.1007/s00382-020-05561-3>, 2021.
- 751 Marcq, S., Laj, P., Roger, J. C., Villani, P., Sellegrì, K., Bonasoni, P., Marinoni, A., Cristofanelli, P., Verza, G. P.,
752 and Bergin, M.: Aerosol optical properties and radiative forcing in the high Himalaya based on measurements at the
753 Nepal Climate Observatory-Pyramid site (5079 m a.s.l.), *Atmos. Chem. Phys.*, 10, 5859–5872,
754 <https://doi.org/10.5194/acp-10-5859-2010>, 2010.
- 755 Matin, M. A., Chitale, V. S., Murthy, M. S. R., Uddin, K., Bajracharya, B., and Pradhan, S.: Understanding forest
756 fire patterns and risk in Nepal using remote sensing, geographic information system and historical fire data, *Int. J.*
757 *Wildland Fire*, 26, 276–286, <https://doi.org/10.1071/WF16056>, 2017.
- 758 Morrison, H., Thompson, G., and Tatarskii, V.: Impact of Cloud Microphysics on the Development of Trailing
759 Stratiform Precipitation in a Simulated Squall Line: Comparison of One- and Two-Moment Schemes, *Mon. Wea.*
760 *Rev.*, 137, 991–1007, <https://doi.org/10.1175/2008MWR2556.1>, 2009.
- 761 Mues, A., Lauer, A., Lupascu, A., Rupakheti, M., Kuik, F., and Lawrence, M. G.: WRF and WRF-Chem v3.5.1
762 simulations of meteorology and black carbon concentrations in the Kathmandu Valley, *Geoscientific Model*
763 *Development*, 11, 2067–2091, <https://doi.org/10.5194/gmd-11-2067-2018>, 2018.
- 764 Nair, V. S., Solmon, F., Giorgi, F., Mariotti, L., Babu, S. S., and Moorthy, K. K.: Simulation of South Asian
765 aerosols for regional climate studies, *Journal of Geophysical Research: Atmospheres*, 117,
766 <https://doi.org/10.1029/2011JD016711>, 2012.
- 767 Napoli, A., Crespi, A., Ragone, F., Maugeri, M., and Pasquero, C.: Variability of orographic enhancement of
768 precipitation in the Alpine region, *Sci Rep*, 9, 13352, <https://doi.org/10.1038/s41598-019-49974-5>, 2019.
- 769 Napoli, A., Desbiolles, F., Parodi, A., and Pasquero, C.: Aerosol indirect effects in complex-orography areas: a
770 numerical study over the Great Alpine Region, *Atmospheric Chemistry and Physics*, 22, 3901–3909,
771 <https://doi.org/10.5194/acp-22-3901-2022>, 2022.
- 772 Palazzi, E., von Hardenberg, J., and Provenzale, A.: Precipitation in the Hindu-Kush Karakoram Himalaya:
773 Observations and future scenarios, *Journal of Geophysical Research: Atmospheres*, 118, 85–100,
774 <https://doi.org/10.1029/2012JD018697>, 2013.
- 775 Palazzi, E., Filippi, L., and von Hardenberg, J.: Insights into elevation-dependent warming in the Tibetan Plateau-
776 Himalayas from CMIP5 model simulations, *Clim Dyn*, 48, 3991–4008, <https://doi.org/10.1007/s00382-016-3316-z>,
777 2017.
- 778 Pepin, N., Bradley, R. S., Diaz, H. F., Baraer, M., Caceres, E. B., Forsythe, N., Fowler, H., Greenwood, G., Hashmi,
779 M. Z., Liu, X. D., Miller, J. R., Ning, L., Ohmura, A., Palazzi, E., Rangwala, I., Schöner, W., Severskiy, I.,
780 Shahgedanova, M., Wang, M. B., Williamson, S. N., Yang, D. Q., and Mountain Research Initiative EDW Working
781 Group: Elevation-dependent warming in mountain regions of the world, *Nature Climate Change*, 5, 424–430,
782 <https://doi.org/10.1038/nclimate2563>, 2015.
- 783 Pincus, R. and Baker, M. B.: Effect of precipitation on the albedo susceptibility of clouds in the marine boundary
784 layer, *Nature*, 372, 250–252, <https://doi.org/10.1038/372250a0>, 1994.
- 785 Prein, A. F. and Heymsfield, A. J.: Increased melting level height impacts surface precipitation phase and intensity,
786 *Nature Climate Change*, 10, 771–776, <https://doi.org/10.1038/s41558-020-0825-x>, 2020.



- 787 Prein, A. F., Langhans, W., Fossler, G., Ferrone, A., Ban, N., Goergen, K., Keller, M., Tölle, M., Gutjahr, O., Feser,
788 F., Brisson, E., Kollet, S., Schmidli, J., Lipzig, N. P. M. van, and Leung, R.: A review on regional convection-
789 permitting climate modeling: Demonstrations, prospects, and challenges, *Reviews of Geophysics*, 53, 323–361,
790 <https://doi.org/10.1002/2014RG000475>, 2015.
- 791 Qian, Y., Yasunari, T. J., Doherty, S. J., Flanner, M. G., Lau, W. K. M., Ming, J., Wang, H., Wang, M., Warren, S.
792 G., and Zhang, R.: Light-absorbing particles in snow and ice: Measurement and modeling of climatic and
793 hydrological impact, *Adv. Atmos. Sci.*, 32, 64–91, <https://doi.org/10.1007/s00376-014-0010-0>, 2015.
- 794 Ramanathan, V. and Carmichael, G.: Global and regional climate changes due to black carbon, *Nature Geosci*, 1,
795 221–227, <https://doi.org/10.1038/ngeo156>, 2008.
- 796 Ramanathan, V., Chung, C., Kim, D., Bettge, T., Buja, L., Kiehl, J. T., Washington, W. M., Fu, Q., Sikka, D. R.,
797 and Wild, M.: Atmospheric brown clouds: Impacts on South Asian climate and hydrological cycle, *Proceedings of*
798 *the National Academy of Sciences*, 102, 5326–5333, <https://doi.org/10.1073/pnas.0500656102>, 2005.
- 799 Rangwala, I. and Miller, J. R.: Climate change in mountains: a review of elevation-dependent warming and its
800 possible causes, *Climatic Change*, 114, 527–547, <https://doi.org/10.1007/s10584-012-0419-3>, 2012.
- 801 Rangwala, I., Miller, J. R., Russell, G. L., and Xu, M.: Using a global climate model to evaluate the influences of
802 water vapor, snow cover and atmospheric aerosol on warming in the Tibetan Plateau during the twenty-first century,
803 *Clim Dyn*, 34, 859–872, <https://doi.org/10.1007/s00382-009-0564-1>, 2010.
- 804 Rosenfeld, D.: TRMM observed first direct evidence of smoke from forest fires inhibiting rainfall, *Geophysical*
805 *Research Letters*, 26, 3105–3108, <https://doi.org/10.1029/1999GL006066>, 1999.
- 806 Rosenfeld, D., Lohmann, U., Raga, G. B., O’Dowd, C. D., Kulmala, M., Fuzzi, S., Reissell, A., and Andreae, M. O.:
807 Flood or Drought: How Do Aerosols Affect Precipitation?, *Science*, 321, 1309–1313,
808 <https://doi.org/10.1126/science.1160606>, 2008.
- 809 Sadavarte, P., Rupakheti, M., Bhave, P., Shakya, K., and Lawrence, M.: Nepal emission inventory – Part I:
810 Technologies and combustion sources (NEEMI-Tech) for 2001–2016, *Atmospheric Chemistry and Physics*, 19,
811 12953–12973, <https://doi.org/10.5194/acp-19-12953-2019>, 2019.
- 812 Saikawa, E., Panday, A., Kang, S., Gautam, R., Zusman, E., Cong, Z., Somanathan, E., and Adhikary, B.: Air
813 Pollution in the Hindu Kush Himalaya, in: *The Hindu Kush Himalaya Assessment: Mountains, Climate Change,*
814 *Sustainability and People*, edited by: Wester, P., Mishra, A., Mukherji, A., and Shrestha, A. B., Springer
815 International Publishing, Cham, 339–387, https://doi.org/10.1007/978-3-319-92288-1_10, 2019.
- 816 Sarangi, C., Tripathi, S. N., Tripathi, S., and Barth, M. C.: Aerosol-cloud associations over Gangetic Basin during a
817 typical monsoon depression event using WRF-Chem simulation, *Journal of Geophysical Research: Atmospheres*,
818 120, 10,974–10,995, <https://doi.org/10.1002/2015JD023634>, 2015.
- 819 Sarangi, C., Qian, Y., Rittger, K., Bormann, K. J., Liu, Y., Wang, H., Wan, H., Lin, G., and Painter, T. H.: Impact of
820 light-absorbing particles on snow albedo darkening and associated radiative forcing over high-mountain Asia: high-
821 resolution WRF-Chem modeling and new satellite observations, *Atmospheric Chemistry and Physics*, 19, 7105–
822 7128, <https://doi.org/10.5194/acp-19-7105-2019>, 2019.
- 823 Shao, T., Liu, Y., Wang, R., Zhu, Q., Tan, Z., and Luo, R.: Role of anthropogenic aerosols in affecting different-
824 grade precipitation over eastern China: A case study, *Science of The Total Environment*, 807, 150886,
825 <https://doi.org/10.1016/j.scitotenv.2021.150886>, 2022.
- 826 Sharma, S., Chen, Y., Zhou, X., Yang, K., Li, X., Niu, X., Hu, X., and Khadka, N.: Evaluation of GPM-Era Satellite
827 Precipitation Products on the Southern Slopes of the Central Himalayas Against Rain Gauge Data, *Remote Sensing*,
828 12, 1836, <https://doi.org/10.3390/rs12111836>, 2020a.



- 829 Sharma, S., Khadka, N., Hamal, K., Shrestha, D., Talchabhadel, R., and Chen, Y.: How Accurately Can Satellite
830 Products (TMPA and IMERG) Detect Precipitation Patterns, Extremities, and Drought Across the Nepalese
831 Himalaya?, *Earth and Space Science*, 7, e2020EA001315, <https://doi.org/10.1029/2020EA001315>, 2020b.
- 832 Shige, S. and Kummerow, C. D.: Precipitation-Top Heights of Heavy Orographic Rainfall in the Asian Monsoon
833 Region, *Journal of the Atmospheric Sciences*, 73, 3009–3024, <https://doi.org/10.1175/JAS-D-15-0271.1>, 2016.
- 834 Sicard, P., Crippa, P., De Marco, A., Castruccio, S., Giani, P., Cuesta, J., Paoletti, E., Feng, Z., and Anav, A.: High
835 spatial resolution WRF-Chem model over Asia: Physics and chemistry evaluation, *Atmospheric Environment*, 244,
836 118004, <https://doi.org/10.1016/j.atmosenv.2020.118004>, 2021.
- 837 Sijikumar, S., Aneesh, S., and Rajeev, K.: Multi-year model simulations of mineral dust distribution and transport
838 over the Indian subcontinent during summer monsoon seasons, *Meteorol Atmos Phys*, 128, 453–464,
839 <https://doi.org/10.1007/s00703-015-0422-0>, 2016.
- 840 Soni, P., Tripathi, S. N., and Srivastava, R.: Radiative effects of black carbon aerosols on Indian monsoon: a study
841 using WRF-Chem model, *Theor Appl Climatol*, 132, 115–134, <https://doi.org/10.1007/s00704-017-2057-1>, 2018.
- 842 Talchabhadel, R., Karki, R., and Parajuli, B.: Intercomparison of precipitation measured between automatic and
843 manual precipitation gauge in Nepal, *Measurement*, 106, 264–273,
844 <https://doi.org/10.1016/j.measurement.2016.06.047>, 2017.
- 845 Terao, T., Islam, Md. N., Hayashi, T., and Oka, T.: Nocturnal jet and its effects on early morning rainfall peak over
846 northeastern Bangladesh during the summer monsoon season, *Geophysical Research Letters*, 33,
847 <https://doi.org/10.1029/2006GL026156>, 2006.
- 848 Tewari, M., Chen, F., Wang, W., Dudhia, J., LeMone, M. A., Mitchell, K., Ek, M., Gayno, G., Wegiel, J., and
849 Cuenca, R. H.: Implementation and verification of the unified NOAA land surface model in the WRF model, in:
850 20th conference on weather analysis and forecasting/16th conference on numerical weather prediction, 2165–2170,
851 2004.
- 852 Twomey, S.: The Influence of Pollution on the Shortwave Albedo of Clouds, *J. Atmos. Sci.*, 34, 1149–1152,
853 [https://doi.org/10.1175/1520-0469\(1977\)034<1149:TIOPOT>2.0.CO;2](https://doi.org/10.1175/1520-0469(1977)034<1149:TIOPOT>2.0.CO;2), 1977.
- 854 Vernier, J.-P., Thomason, L. W., and Kar, J.: CALIPSO detection of an Asian tropopause aerosol layer, *Geophysical
855 Research Letters*, 38, <https://doi.org/10.1029/2010GL046614>, 2011.
- 856 Wang, S., Zhang, M., Pepin, N. C., Li, Z., Sun, M., Huang, X., and Wang, Q.: Recent changes in freezing level
857 heights in High Asia and their impact on glacier changes, *Journal of Geophysical Research: Atmospheres*, 119,
858 1753–1765, <https://doi.org/10.1002/2013JD020490>, 2014.
- 859 Wu, L., Su, H., and Jiang, J. H.: Regional simulation of aerosol impacts on precipitation during the East Asian
860 summer monsoon, *Journal of Geophysical Research: Atmospheres*, 118, 6454–6467,
861 <https://doi.org/10.1002/jgrd.50527>, 2013.
- 862 Wu, L., Gu, Y. (ORCID:0000000234120794), Jiang, J. H., Su, H., Yu, N., Zhao, C., Qian, Y., Zhao, B.
863 (ORCID:0000000184389188), Liou, K.-N., and Choi, Y.-S.: Impacts of aerosols on seasonal precipitation and
864 snowpack in California based on convection-permitting WRF-Chem simulations, *Atmospheric Chemistry and
865 Physics (Online)*, 18, <https://doi.org/10.5194/acp-18-5529-2018>, 2018.
- 866 Yang, Q., W. I. Gustafson Jr., Fast, J. D., Wang, H., Easter, R. C., Morrison, H., Lee, Y.-N., Chapman, E. G., Spak,
867 S. N., and Mena-Carrasco, M. A.: Assessing regional scale predictions of aerosols, marine stratocumulus, and their
868 interactions during VOCALS-REx using WRF-Chem, *Atmos. Chem. Phys.*, 11, 11951–11975,
869 <https://doi.org/10.5194/acp-11-11951-2011>, 2011.



- 870 Zaveri, R. A. and Peters, L. K.: A new lumped structure photochemical mechanism for large-scale applications,
871 *Journal of Geophysical Research: Atmospheres*, 104, 30387–30415, <https://doi.org/10.1029/1999JD900876>, 1999.
- 872 Zaveri, R. A., Easter, R. C., Fast, J. D., and Peters, L. K.: Model for Simulating Aerosol Interactions and Chemistry
873 (MOSAIC), *Journal of Geophysical Research: Atmospheres*, 113, <https://doi.org/10.1029/2007JD008782>, 2008.
- 874 Zhang, Y. and Guo, Y.: Variability of atmospheric freezing-level height and its impact on the cryosphere in China,
875 *Annals of Glaciology*, 52, 81–88, <https://doi.org/10.3189/172756411797252095>, 2011.
- 876 Zhang, Y., Fan, J., Li, Z., and Rosenfeld, D.: Impacts of cloud microphysics parameterizations on simulated
877 aerosol–cloud interactions for deep convective clouds over Houston, *Atmospheric Chemistry and Physics*, 21, 2363–
878 2381, <https://doi.org/10.5194/acp-21-2363-2021>, 2021.
- 879 Zhao, C., Chen, S., Leung, L. R., Qian, Y., Kok, J. F., Zaveri, R. A., and Huang, J.: Uncertainty in modeling dust
880 mass balance and radiative forcing from size parameterization, *Atmospheric Chemistry and Physics*, 13, 10733–
881 10753, <https://doi.org/10.5194/acp-13-10733-2013>, 2013.
- 882 Zhao, C., Hu, Z., Qian, Y., Ruby Leung, L., Huang, J., Huang, M., Jin, J., Flanner, M. G., Zhang, R., Wang, H.,
883 Yan, H., Lu, Z., and Streets, D. G.: Simulating black carbon and dust and their radiative forcing in seasonal snow: a
884 case study over North China with field campaign measurements, *Atmospheric Chemistry and Physics*, 14, 11475–
885 11491, <https://doi.org/10.5194/acp-14-11475-2014>, 2014.
- 886
- 887



888 **Table 1** Model configuration.

Physics option	Scheme
Microphysics	Morrison-2 moment (Morrison et al., 2009)
Radiation	Rapid Radiative Transfer Model for General Circulation Models (RRTMG; Iacono et al., 2008)
Land surface	Unified Noah (Tewari et al., 2004)
Planetary Boundary layer	Yonsei University (YSU; Hong et al., 2006)
Cumulus	Grell-3D for 9 km (Grell and Dévényi, 2002) and turned off for 3 km grid size nested domain.
Chemical and Aerosol mechanism	CBM-Z and MOSAIC-4bin
Boundary Condition	ERA5 (meteorology) and CAM-Chem (Chemistry)

889

890



891

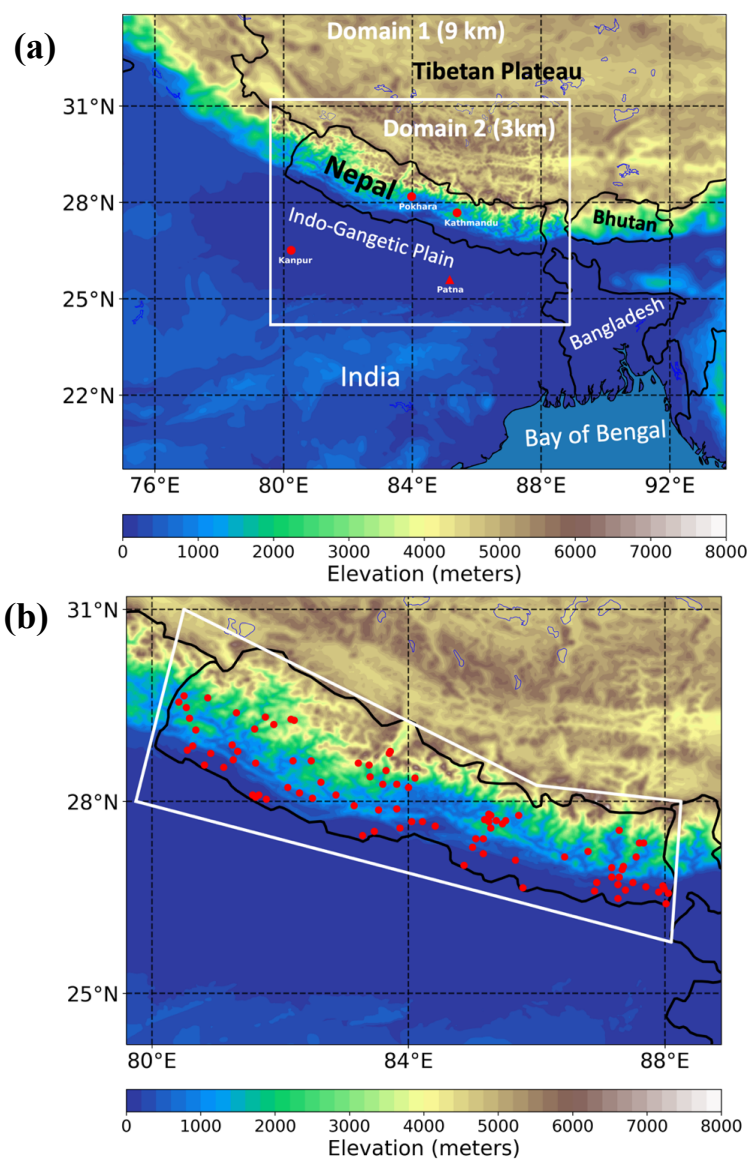


Figure 1 (a) The topography of the 9 km and 3 km nested grid size domains used in the simulation. The red marker represents the station locations for AERONET (circle) and upper air sounding (triangle). (b) The white-colored polygon represents the Central Himalayan region (CenHim) mentioned in the text. The red marker represents the locations of DHM Nepal rain gauge stations.

892

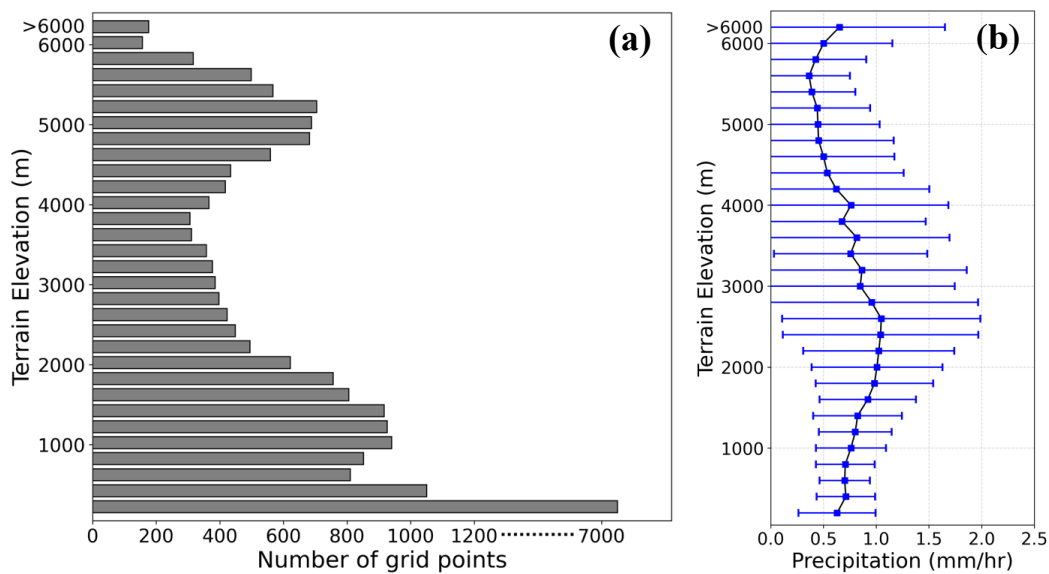


Figure 2 (a) The total number of grids per elevation range for 200 m bins up to 6000 m and one bin above 6000 m. (b) Variation of CTL mean (± 1 standard deviation) precipitation over the CenHim as a function of altitude.

893

894



895

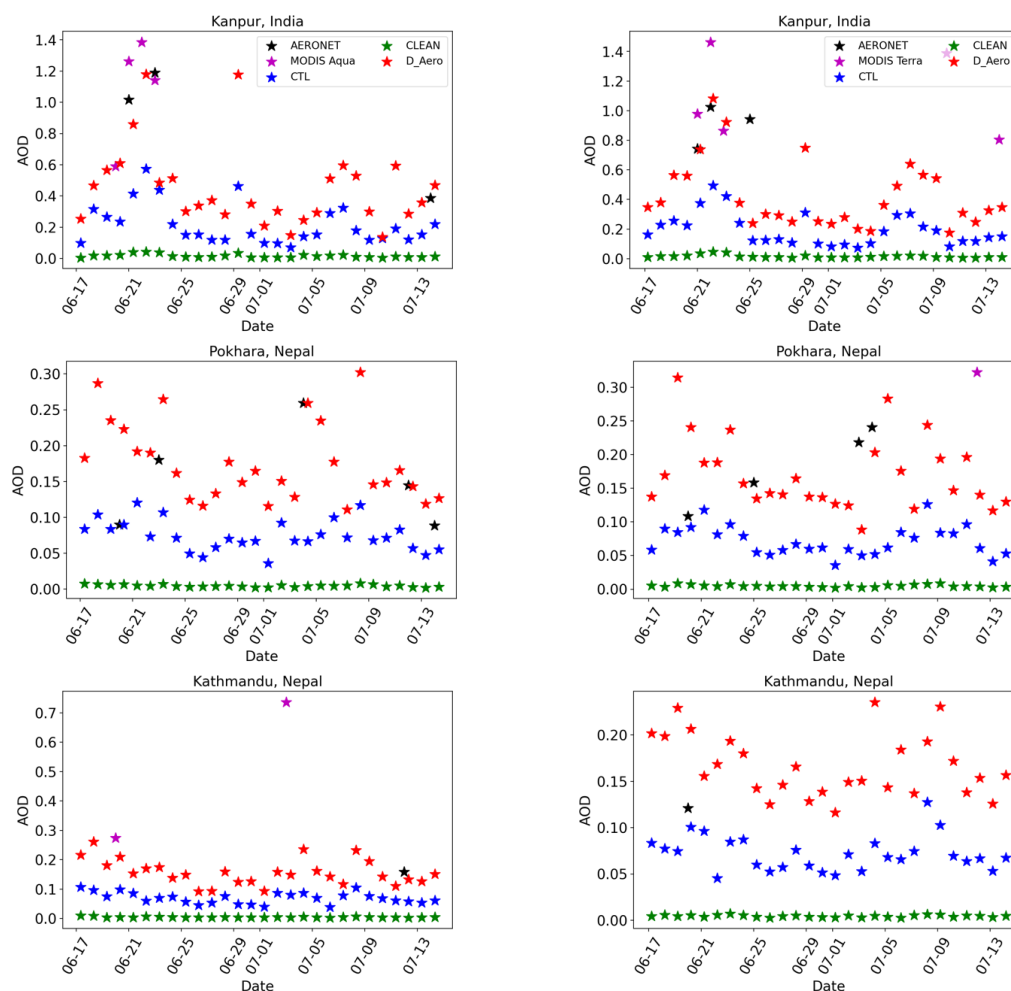


Figure 3 The simulated AERONET and MODIS Aqua (first column) and Terra (second column) AOD at three AERONET stations (Kanpur, Pokhara, and Kathmandu; see Fig. 1a for location).

896

897

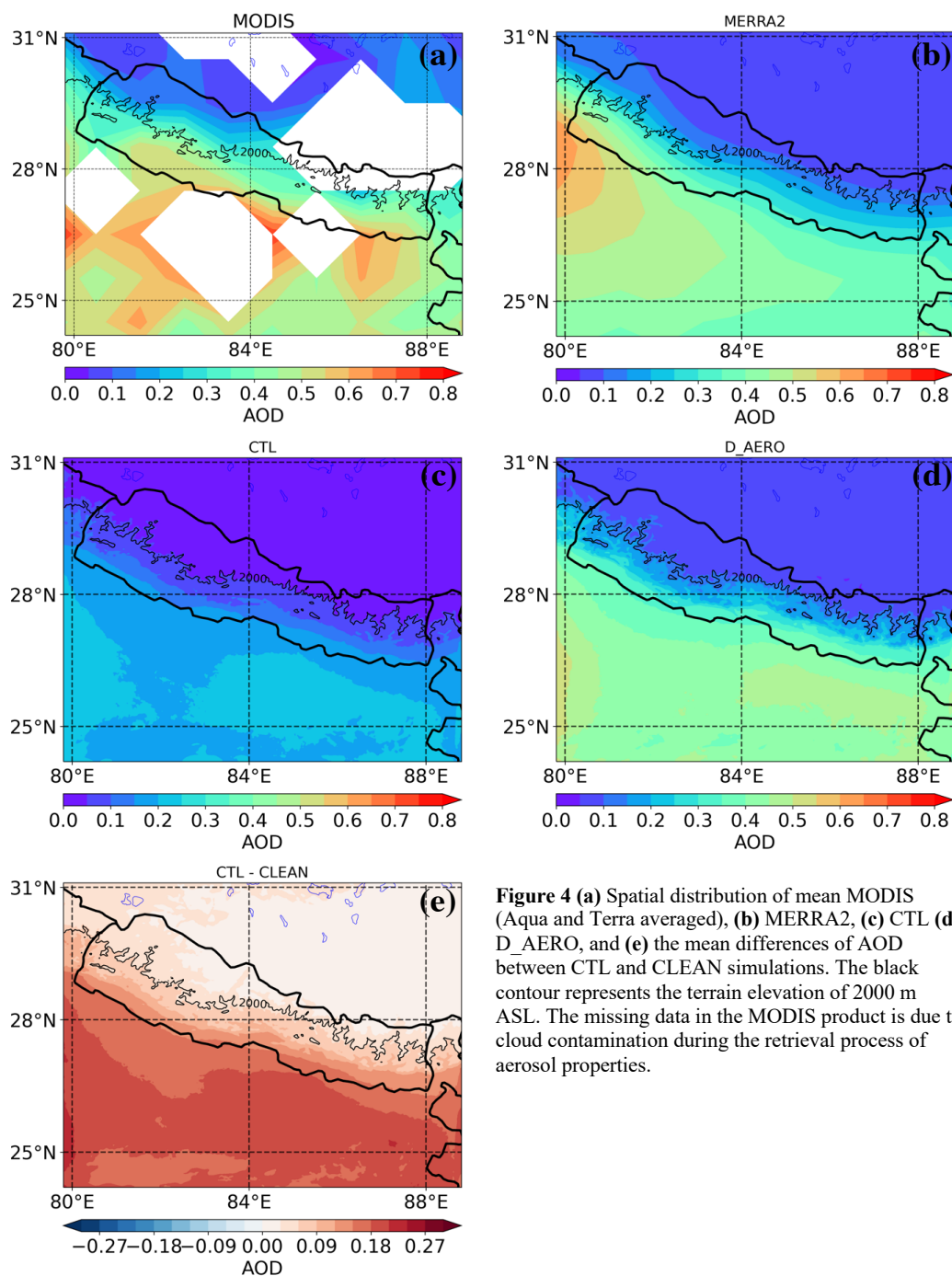


Figure 4 (a) Spatial distribution of mean MODIS (Aqua and Terra averaged), (b) MERRA2, (c) CTL (d) D_AERO, and (e) the mean differences of AOD between CTL and CLEAN simulations. The black contour represents the terrain elevation of 2000 m ASL. The missing data in the MODIS product is due to cloud contamination during the retrieval process of aerosol properties.

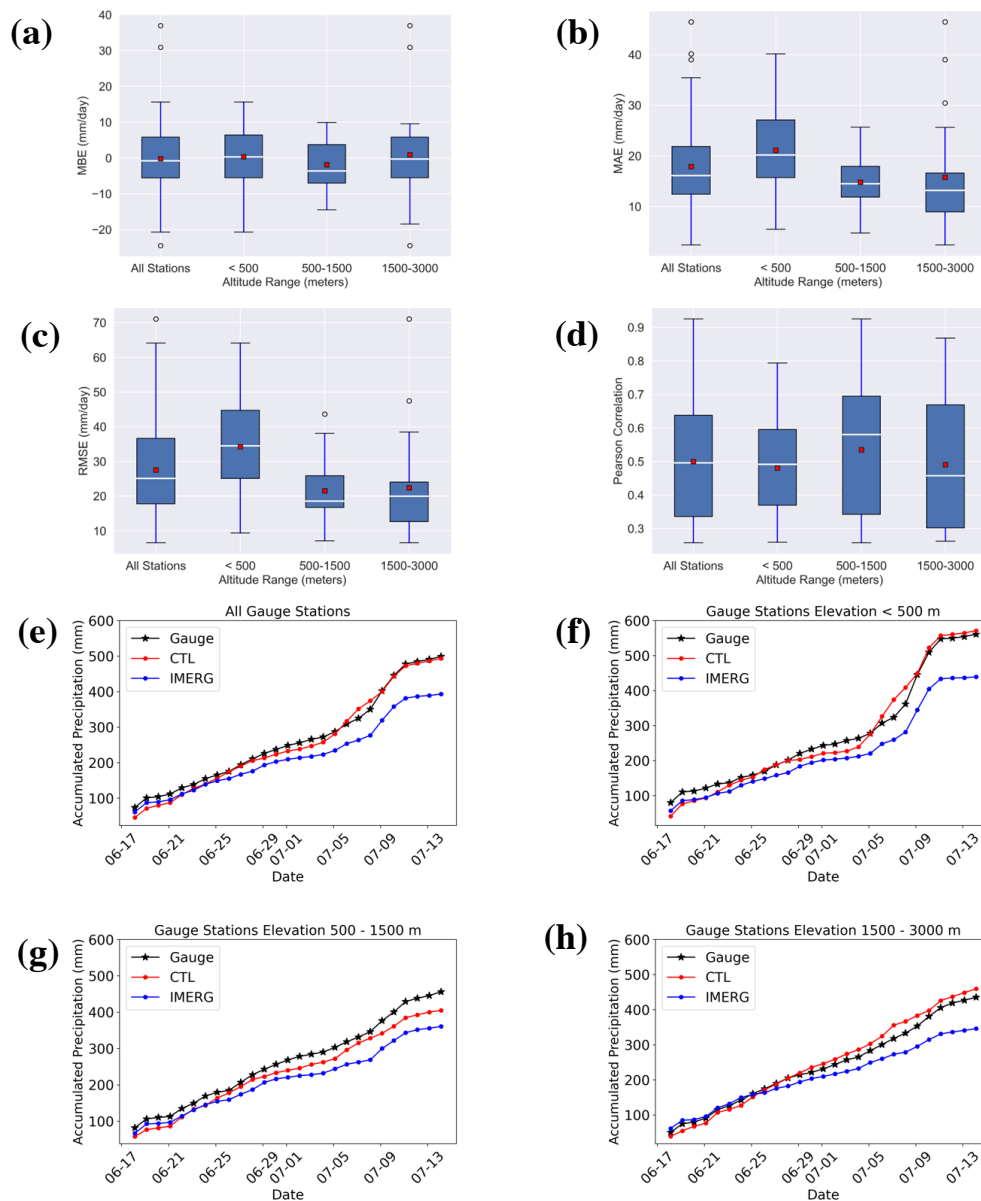


Figure 5 Box plots show the median, interquartile range, and extreme distribution for each of the error statistics [(a) MBE, (b) MAE, (c) RMSE, and (d) Pearson correlation] between the simulated and the rain gauge stations over Nepal, at an altitude that ranges below 500 m (41 stations), between 500 and 1500 m (28 stations), and between 1500 and 3000 m (21 stations). The red color marker at the center of the box represents the mean value. Time series of averaged accumulated precipitation at DHM rain gauge stations, CTL, and IMERG; (e) all rain gauge stations, stations located (f) below 500 m ASL, (g) between 500 and 1500 m, and (h) between 1500 and 3000 m terrain elevation.

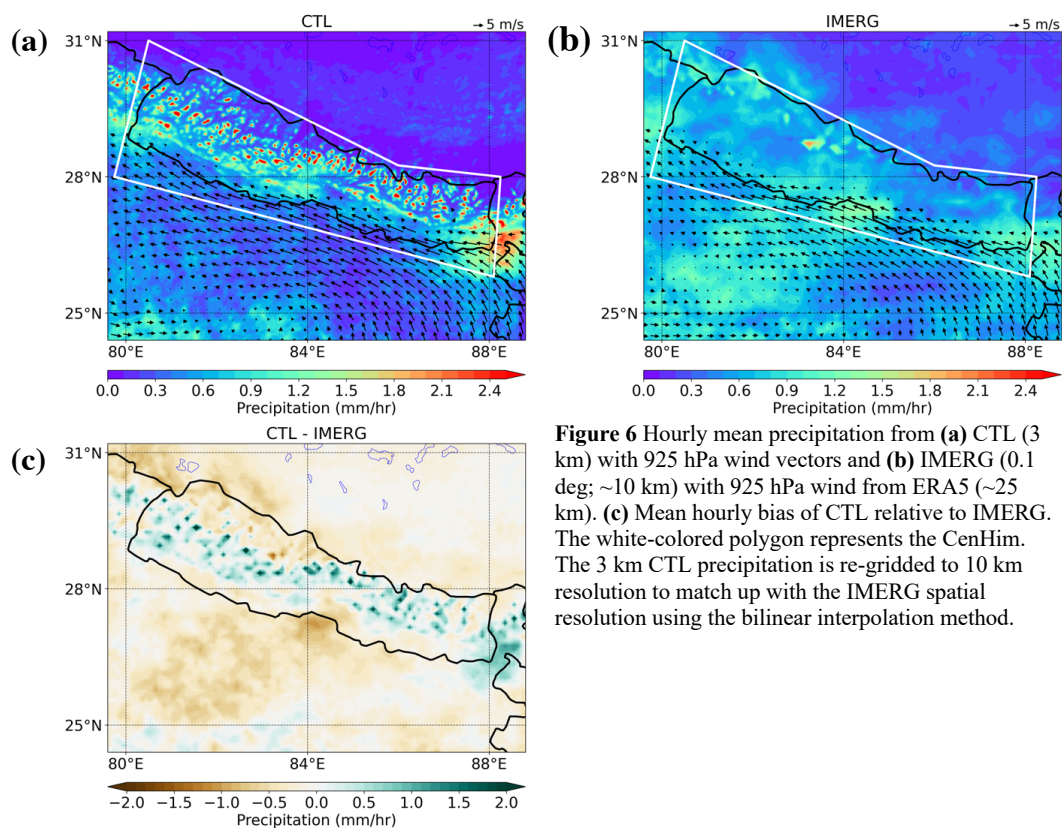


Figure 6 Hourly mean precipitation from (a) CTL (3 km) with 925 hPa wind vectors and (b) IMERG (0.1 deg; ~10 km) with 925 hPa wind from ERA5 (~25 km). (c) Mean hourly bias of CTL relative to IMERG. The white-colored polygon represents the CenHim. The 3 km CTL precipitation is re-gridded to 10 km resolution to match up with the IMERG spatial resolution using the bilinear interpolation method.

900

901



902

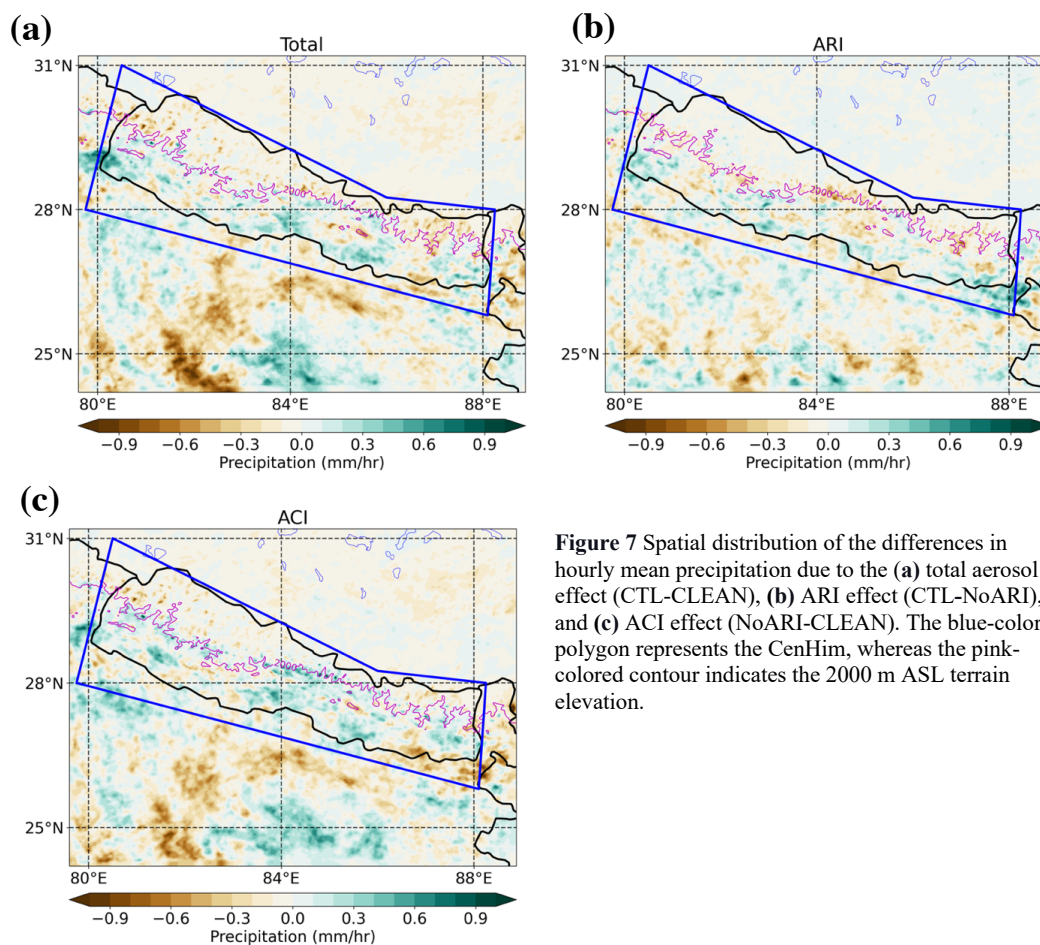


Figure 7 Spatial distribution of the differences in hourly mean precipitation due to the (a) total aerosol effect (CTL-CLEAN), (b) ARI effect (CTL-NoARI), and (c) ACI effect (NoARI-CLEAN). The blue-colored polygon represents the CenHim, whereas the pink-colored contour indicates the 2000 m ASL terrain elevation.

903

904



905

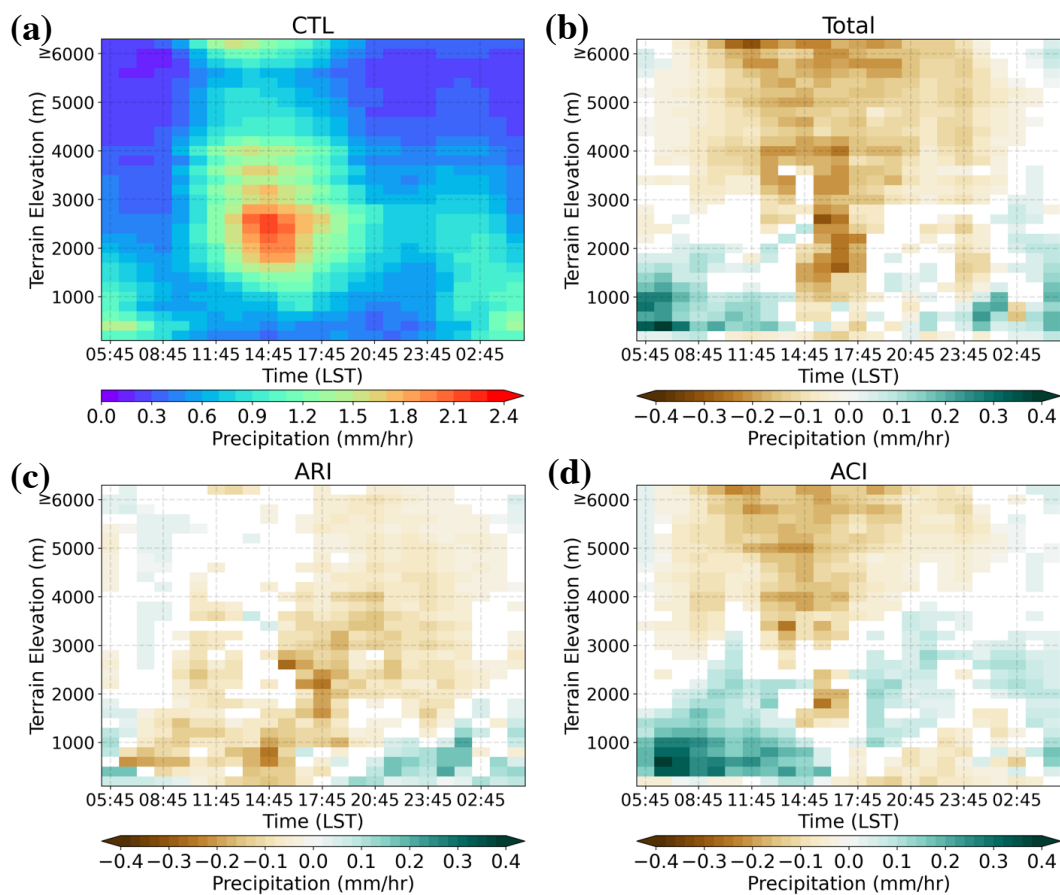


Figure 8 Diurnal-elevation (a) CTL precipitation, (b) aerosol effect (CTL-CLEAN), (c) ARI effect (CTL-NoARI), and (d) ACI effect (NoARI-CLEAN) and their diurnal variability. Only the differences that are significant at the 90 % confidence level based on the student t-test are plotted.

906

907

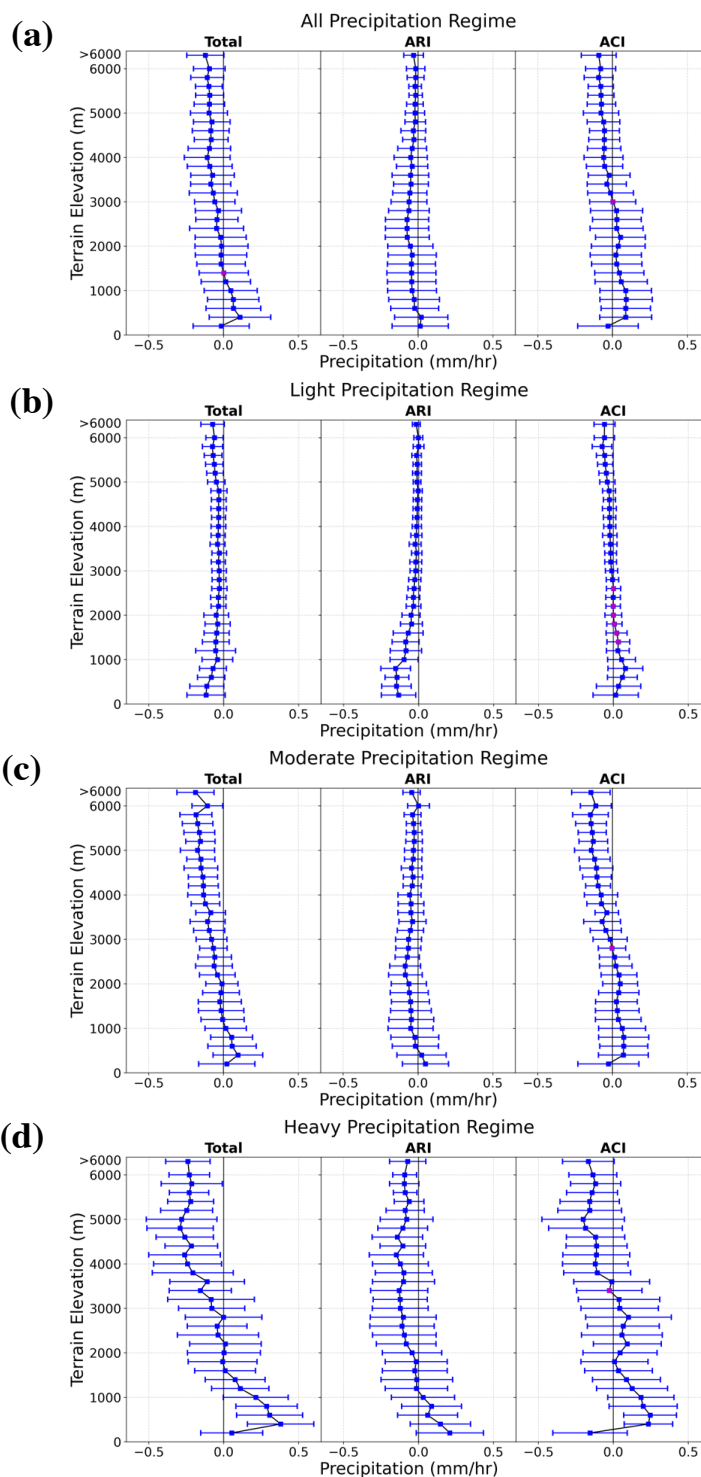




Figure 9 Elevational variability in different regimes [(a) all, (b) light, (c) moderate, and (d) heavy] precipitation differences due to aerosols. The blue dots and error bars represent the mean and ± 1 standard deviation. The pink dot indicates that the differences between the two simulations are not significant at the 90% confidence interval based on the student t-test.

908

909



910

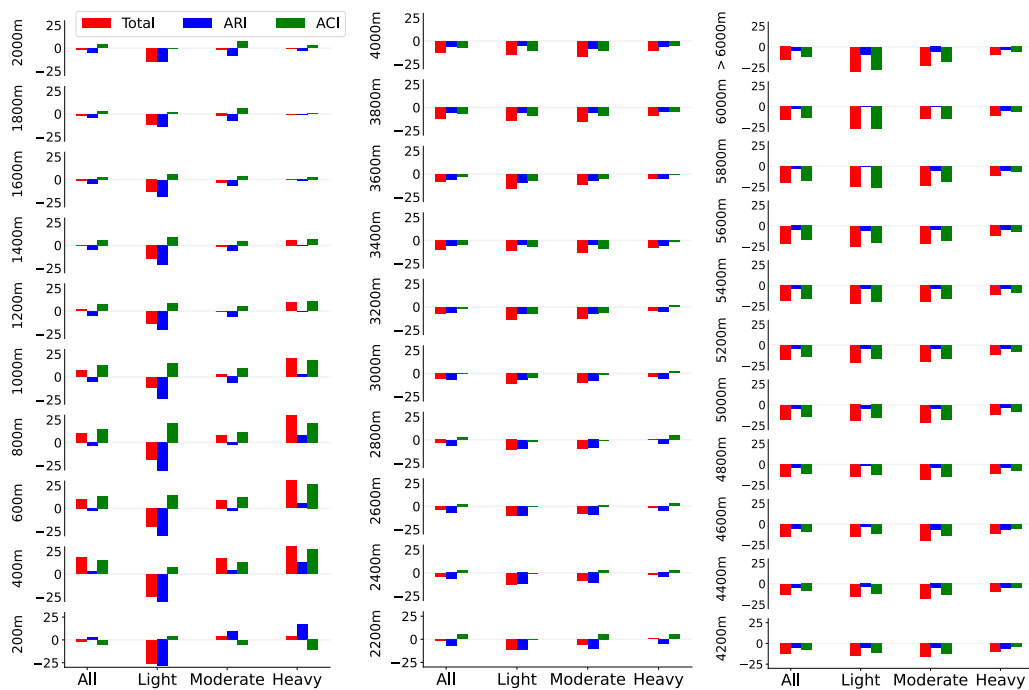


Figure 10 Relative change (%) in precipitation due to different effects of aerosols for all the elevational bins.

911

912



913

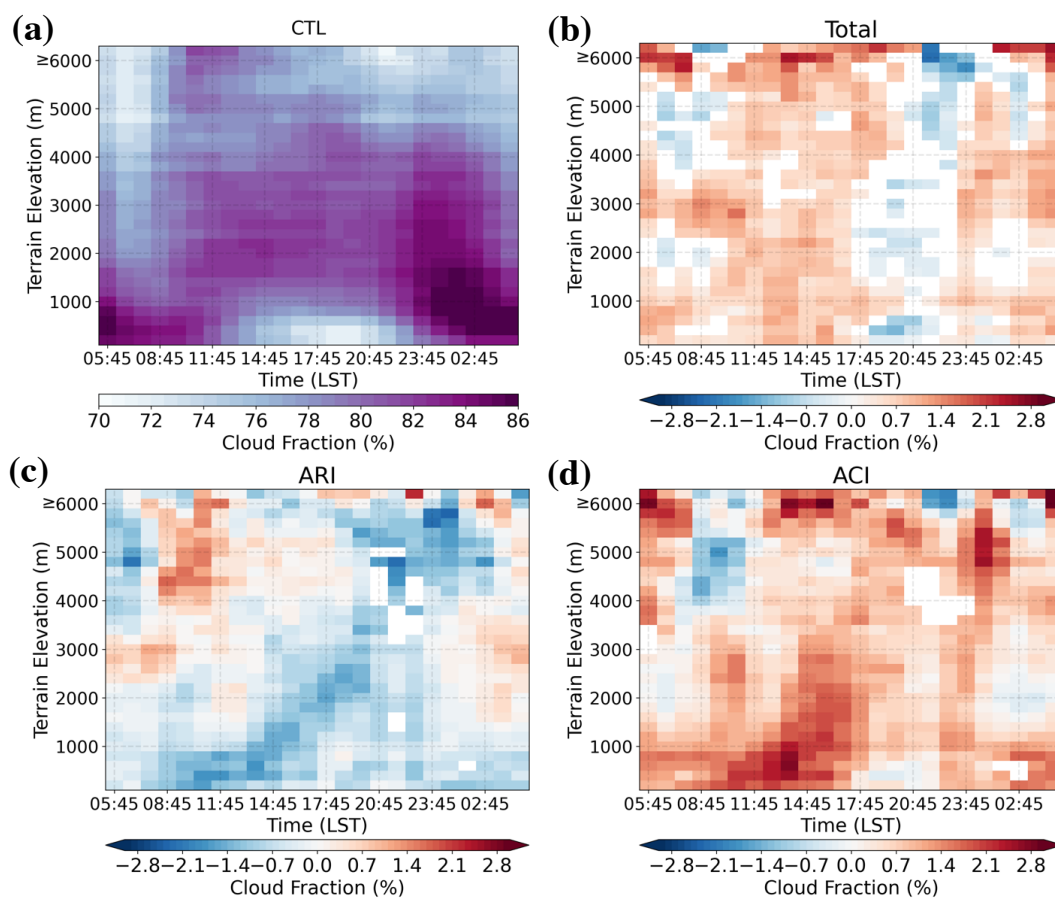


Figure 11 Diurnal-elevation of cloud fraction (a) CTL, and due to (b) aerosol effect (CTL-CLEAN), (c) ARI effect (CTL-NoARI), and (d) ACI effect (NoARI-CLEAN) and their diurnal variability. Only the differences that are significant at the 90 % confidence level based on the student t-test are plotted.

914

915



916

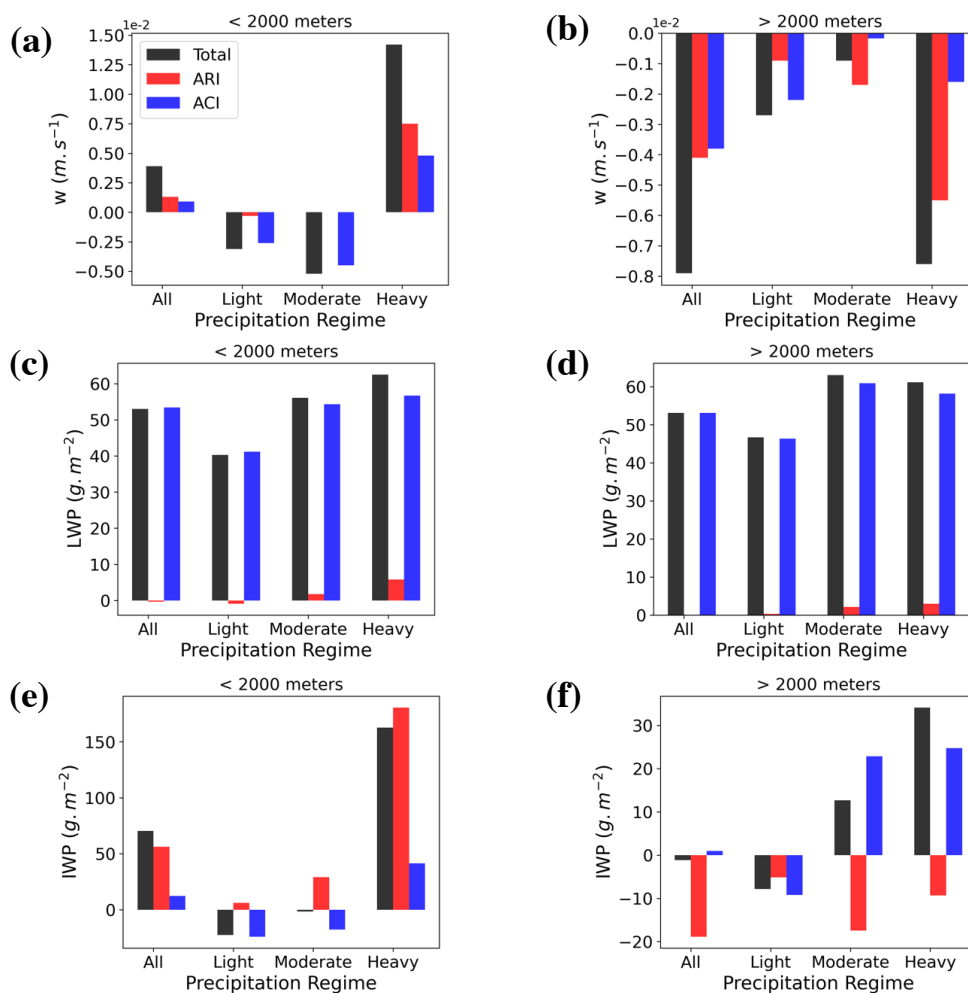


Figure 12 Monthly mean perturbation of (a, b) vertical velocity, (c, d) LWP, and (e, f) IWP over the CenHim region for the terrain elevation below (first column) and above (second column) surface elevation of 2000 m ASL, for total, light, moderate, and heavy precipitation regime.

917

918



919

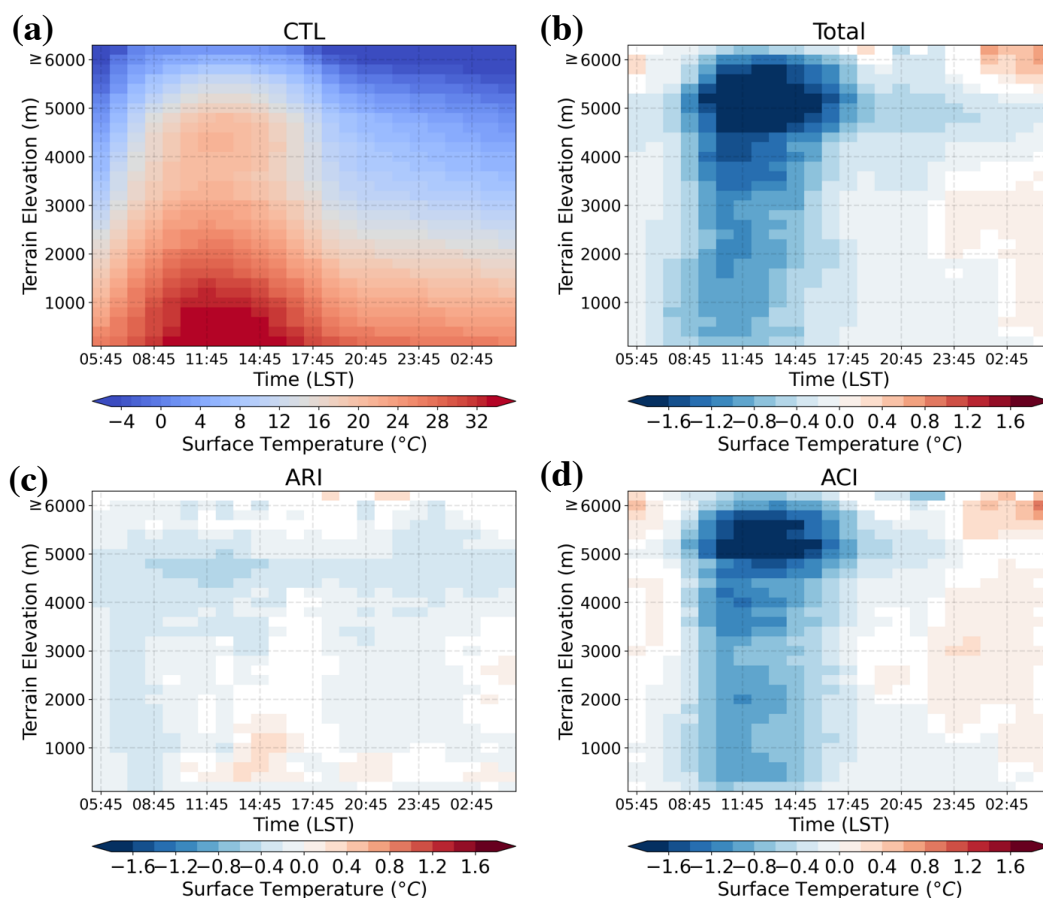


Figure 13 Diurnal-elevation of temperature (a) CTL simulated, and due to (b) aerosol effect (CTL-CLEAN), (c) ARI effect (CTL-NoARI), and (d) ACI effect (NoARI-CLEAN) and their diurnal variability. Only the differences that are significant at the 90 % confidence level based on the student t-test are plotted.

920

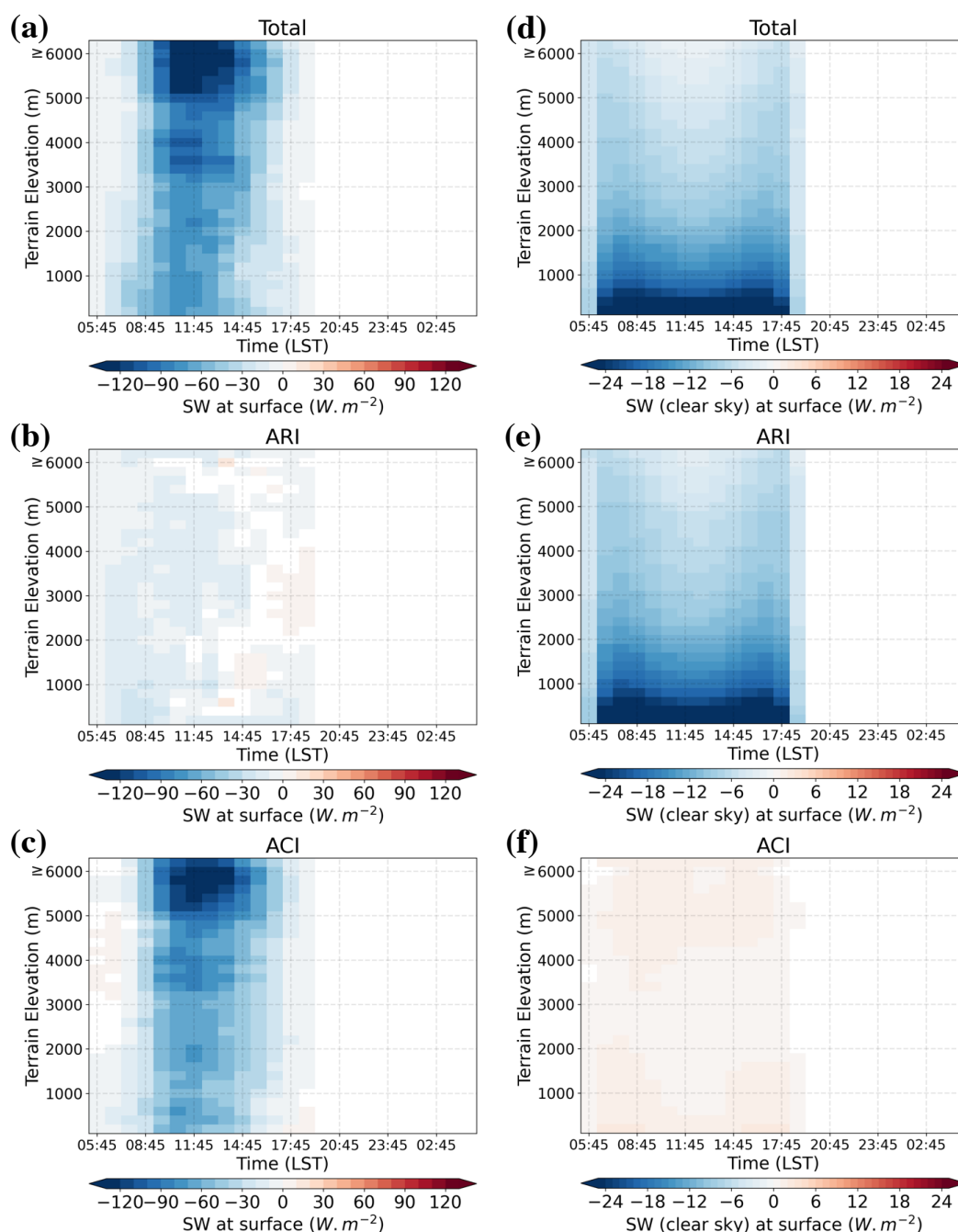


Figure 14 Diurnal-elevation all-sky (first column) and clear-sky (second column) downwelling shortwave radiation at the surface due to (a, c) aerosol effect (CTL-CLEAN), (b, d) ARI effect (CTL-NoARI), and (e, f) ACI effect (NoARI-CLEAN) and their diurnal variability. Only the differences that are significant at the 90 % confidence level based on the student t-test are plotted.



923

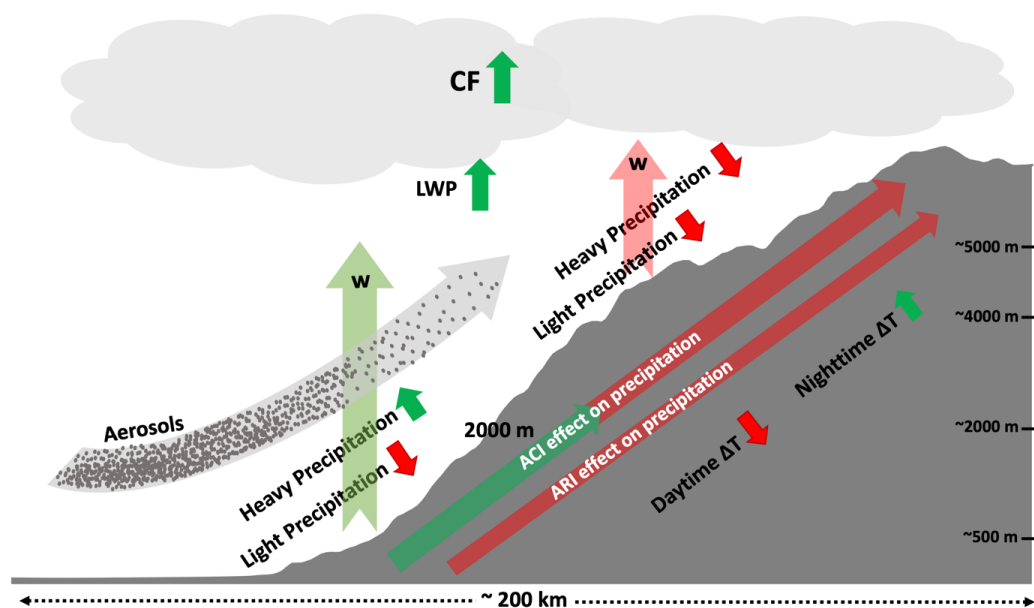


Figure 15 Schematic representing the relative impact of the different effects of aerosols on elevation-dependent precipitation. Green and red arrows represent the increasing and decreasing magnitude of different parameters, respectively. The shaded grey area represents the characteristic elevation of the southern slopes across the Central Himalayan region.

924